LJMU Research Online

Park, G, Currie, MJ, Thomas, HS, Rosolowsky, E, Dempsey, JT, Kim, KT, Rigby, AJ, Su, Y, Eden, DJ, Colombo, D, Parsons, H and Moore, TJT

 12CO (3–2) High-Resolution Survey (COHRS) of the Galactic Plane: Complete Data Release

https://researchonline.ljmu.ac.uk/id/eprint/19118/

Article

¹²CO (3–2) High-Resolution Survey (COHRS) of the Galactic Plane: Complete Data Release

Geumsook Park (박금숙)[1] , Malcolm J. Currie[2,3] , Holly S. Thomas[4] , Erik Rosolowsky[5] , Jessica T. Dempsey[2,6] ,
Kee-Tae Kim[1,7] , Andrew J. Rigby[8,9] , Yang Su[10] , David J. Eden[11,12] , Dario Colombo[13], Harriet Parsons[2] , and
Toby J. T. Moore[11]

[1] Korea Astronomy and Space Science Institute, 776 Daedeokdae-ro, Yuseong-gu, Daejeon 34055, Republic of Korea; pgsook@gmail.com
[2] East Asian Observatory, 660 N. A'ohōkū Place, HI 96720, USA
[3] RAL Space, STFC Rutherford Appleton Laboratory, Chilton, Didcot, Oxfordshire OX11 0QX, UK
[4] Radio Telescope Data Center, Center for Astrophysics, Harvard & Smithsonian, 60 Garden Street, Cambridge, MA 02138, USA
[5] Department of Physics, University of Alberta, 4-181 CCIS, Edmonton, AB T6G 2E1, Canada
[6] ASTRON, Oude Hoogeveensedijk 4, 7991 PD Dwingeloo, The Netherlands
[7] University of Science and Technology, Korea (UST), 217 Gajeong-ro, Yuseong-gu, Daejeon 34113, Republic of Korea
[8] School of Physics and Astronomy, Cardiff University, Cardiff CF24 3AA, UK
[9] School of Physics and Astronomy, University of Leeds, Leeds LS2 9JT, UK
[10] Purple Mountain Observatory and Key Laboratory of Radio Astronomy, Chinese Academy of Sciences, Nanjing 210034, People's Republic of China
[11] Astrophysics Research Institute, Liverpool John Moores University, IC2, Liverpool Science Park, 146 Brownlow Hill, Liverpool L3 5RF, UK
[12] Armagh Observatory and Planetarium, College Hill, Armagh BT61 9DG, UK
[13] Max Planck Institute for Radioastronomy, Auf dem Hügel 69, D-53121 Bonn, Germany
Received 2022 July 31; revised 2022 October 2; accepted 2022 October 3; published 2022 December 29

Abstract

We present the full data release of the ¹²CO (3–2) High-Resolution Survey (COHRS), which has mapped the inner Galactic plane over the range of $9°.5 \leqslant l \leqslant 62°.3$ and $|b| \leqslant 0°.5$. COHRS has been carried out using the Heterodyne Array Receiver Program on the 15 m James Clerk Maxwell Telescope in Hawaii. The released data are smoothed to have a spatial resolution of $16''.6$ and a velocity resolution of $0.635 \, \mathrm{km \, s^{-1}}$, achieving a mean rms of ~ 0.6 K on T_A^*. The COHRS data are useful for investigating detailed three-dimensional structures of individual molecular clouds and large-scale structures such as spiral arms in the Galactic plane. Furthermore, data from other available public surveys of different CO isotopologues and transitions with similar angular resolutions to this survey, such as FUGIN, SEDIGISM, and CHIMPS/CHIMPS2, allow studies of the physical properties of molecular clouds and comparison of their states. In this paper, we report further observations on the second release and improved data reduction since the original COHRS release. We discuss the characteristics of the COHRS data and present integrated-emission images and a position–velocity (PV) map of the region covered. The PV map shows a good match with spiral-arm traces from existing CO and H I surveys. We also obtain and compare integrated one-dimensional distributions of ¹²CO (1–0) and (3–2) and those of star-forming populations.

Unified Astronomy Thesaurus concepts: Molecular clouds (1072)

1. Introduction

Carbon monoxide (CO) is essential for tracing the molecular interstellar medium (ISM) and understanding its physical properties. Molecular hydrogen (H_2) is the most abundant molecule in the ISM, but due to its symmetry and low molecular weight, there is a lack of transitions with energies that are excited under standard molecular ISM conditions with $T \sim 10$–100 K. As the second most abundant molecule, CO is the best tracer of the bulk of the molecular ISM. Its rotational (J) transitions trace different conditions in the ISM. Cold gas preferentially emits mostly in the $J = (1-0)$ line, and warmer, denser gas radiates more in higher-J lines. Different CO isotopologues reflect opacity effects. ¹²CO is the most abundant CO isotopologue, which produces strong emission lines from most of the molecular gas in the ISM. ¹³CO and C¹⁸O are less abundant and therefore fainter than ¹²CO, but trace optically thinner emission in most cases of low excitation temperature. So ¹²CO traces where the molecular gas is, while ¹³CO and C¹⁸O provide a view of the optically thickest gas. Thus,

observations of different CO isotopologues and transitions are complementary.

While continuum tracers blend emission along the line of sight, the high spectral resolution and Doppler effect of CO line emission allow us to identify discrete features in velocity that map to distance, although there is kinematic ambiguity within the solar circle in position–position–velocity (PPV) space. Also, CO is often used as a mass tracer, even though the emissivity per unit mass (that is, the X-factor) is variable (Bolatto et al. 2013). Therefore, CO is useful for investigating detailed information about the morphological, physical, and kinematic properties of molecular clouds.

Molecular gas is predominantly distributed in the disks of late-type galaxies, including the Milky Way. It traces large-scale galactic structures such as spiral arms, giant molecular clouds (GMCs), and star-forming regions. Significant efforts have long been made to provide targeted surveys of the Galactic plane in several CO isotopologues and transitions by using a variety of facilities. Since the molecular gas in the Milky Way is centrally concentrated, CO surveys in the Milky Way usually focus on the first and fourth Galactic quadrants. Table 1 presents examples of Galactic CO surveys in which the first quadrant is within the scope of the survey. The early observations from the University of

Table 1
Examples of CO Surveys That Include the First Galactic Quadrant

Survey Name	Molecule(s)	Survey Coverage (deg)		Telescope(s)	Angular Sampling (arcseconds)	Angular Resolution[a] (arcseconds)	Velocity Resolution[a] (km s^{-1})	rms Sensitivity[b] (K)	References[c]
UMSB	$^{12}CO(J=1-0)$	$l=+8-+90$	$\|b\| \lesssim 1.05$	FCRAO	180–360	45	0.65/1	~0.6	1
CfA	$^{12}CO(J=1-0)$	$l=-180-+180$	$\|b\| \lesssim 10-30$	CfA/ Chile/NY	225–450	504–528	0.65	~0.1–0.4	2
GRS	$^{13}CO(J=1-0)$	$l=+18-+55$	$\|b\| \lesssim 1$	FCRAO	22	46	0.21	~0.1	3
FUGIN	$^{12}CO/^{13}CO/C^{18}O(J=1-0)$	$l=+10-+50,$ $+198-+236$	$\|b\| \lesssim 1$	Nobeyama	8.5	~14/~20	0.65/1.3	~1.7/0.8/0.8	4
MWISP I+II[d]	$^{12}CO/^{13}CO/C^{18}O(J=1-0)$	$l=+10-+240$	$\|b\| \lesssim 10.25$	PMO	15	~50	~0.16	~0.2/0.1/0.1	5, 6
SEDIGISM	$^{13}CO/C^{18}O(J=2-1)$	$l=-60-+18$	$\|b\| \lesssim 0.5$	APEX	15	28/30	~0.1/0.25	~0.4/0.4	7
COHRS	$^{12}CO(J=3-2)$	$l=+9.5-+62.3$	$\|b\| \lesssim 0.5$	JCMT	6	13.8/16.6	0.42/0.635	~0.8/0.8	8, 9
CHIMPS	$^{13}CO/C^{18}O(J=3-2)$	$l=+28-+46$	$\|b\| \lesssim 0.5$	JCMT	7.3	15	0.055/0.5	~0.6/0.7	10
CHIMPS2	$^{12}CO/^{13}CO/C^{18}O(J=3-2)$	$l=-5-+28$ $l=+215-+225$	$\|b\| \lesssim 0.5$ $-2 \leqslant b \leqslant 0$	JCMT	e	e	e	~1.0/.../...	11

Notes.
[a] If two values connected by a slash (/) are provided, the first is the raw value and the other is the value after smoothing. Otherwise, a single entry is a raw value.
[b] Estimated rms noise level (T_{mb}) at a velocity channel width of 1 km s^{-1} and a given original angular resolution.
[c] References: (1) Sanders et al. (1986), (2) Dame et al. (2001), (3) Jackson et al. (2006), (4) Umemoto et al. (2017), (5) Su et al. (2019), (6) Yuan et al. (2022), (7) Schuller et al. (2017), (8) Dempsey et al. (2013), (9) this work, (10) Rigby et al. (2016), (11) Eden et al. (2020).
[d] The MWISP I project ($l = +10°-+230°$, $\|b\| \lesssim 5.25$) was completed over a 10 yr period from 2011 to 2021. The MWISP group plans to extend the Galactic latitude to $b = \pm10.25$, i.e., the MWISP II project for the $l = +10°-+240°$ and $\|b\| \lesssim 10.25$ region along the Galactic plane.
[e] For ^{12}CO and $^{13}CO/C^{18}O$ observations, CHIMPS observing strategies followed that of COHRS.

Massachusetts–Stony Brook (UMSB) survey (Sanders et al. 1986), the CfA survey (Dame et al. 2001), and the Boston University–Five College Radio Astronomy Observatory Galactic Ring Survey (Jackson et al. 2006) provide ^{12}CO (1–0) or ^{13}CO (1–0) emission data. In particular, since the CfA survey covers the entire Galactic plane, it is still important for understanding the large-scale distribution of molecular gas, although the angular resolution of the survey data is low by modern standards.

Surveys in recent years have simultaneously observed multiple lines of CO isotopologues at moderate or much higher angular resolutions. For example, there are the FOREST Unbiased Galactic Plane Imaging Survey (FUGIN; Umemoto et al. 2017), the Milky Way Imaging Scroll Painting (MWISP) I and II projects (e.g., see Su et al. 2019; Yuan et al. 2022), and the Structure, Excitation, and Dynamics of the Inner Galactic[14] Interstellar Medium (SEDIGISM) survey (Schuller et al. 2017). In addition, two surveys that used the JCMT measured the (3–2) transition lines of three CO isotopologues (^{12}CO/^{13}CO/C^{18}O). For ^{12}CO, the CO High-Resolution Survey (COHRS), of which the first release (R1) was presented by Dempsey et al. (2013, hereafter Paper I) and the second release (R2) is described in this paper, has been carried out. For ^{13}CO and C^{18}O, the CO Heterodyne Inner Milky Way Plane Survey (CHIMPS; Rigby et al. 2016) mapped part of the regions covered by COHRS. An extension of this survey, CHIMPS2, is now proceeding to extend into lower Galactic longitudes, and to cover the Galactic center and an outer region (Eden et al. 2020). These recent surveys provide significantly improved CO data in angular resolution compared with the CfA survey. Specifically, about 1000 times the area of the COHRS beam is equal to one CfA beam area.

COHRS observes ^{12}CO (3–2), which is optically thinner compared with lower transition lines of the same isotopologue and is seen at a higher frequency, resulting in higher-resolution data given the same telescope diameter. Compared with ^{12}CO (1–0), ^{12}CO (3–2) is excited in a warmer (energy above ground (E_u/k_B): 5.5 K for $J = 1$, 33 K for $J = 3$) and denser (critical density: $\sim 2 \times 10^3$ cm^{-3} for (1–0), $\sim 5 \times 10^4$ cm^{-3} for (3–2) in the optically thin regime) environment. This transition traces molecular clouds, particularly gas that is likely to be more strongly associated with star-forming regions. It is also an excellent tracer of outflow activity, which generally indicates the very early stages of star formation (Banerjee & Pudritz 2006). Using the COHRS R1 data, Li et al. (2018) established a catalog of high-mass outflows associated with ATLASGAL clumps, resulting in a detection rate of 22%. Colombo et al. (2019) analyzed integrated properties of molecular clouds by applying the Spectral Clustering for Interstellar Molecular Emission Segmentation algorithm (Colombo et al. 2015). They identified 85,020 clouds and found that 35% of the classified clouds are located within spiral arms, assuming arm widths of 600 pc (Vallee 2017). They derived mass and size distributions showing a power-law relationship with spectral indices of -1.75 and -2.80, respectively, and the distributions are truncated at $\sim 3 \times 10^6 \, M_\odot$ and ~ 70 pc, respectively.

COHRS can be compared with other Galactic large-scale surveys at submillimeter and infrared wavelengths to study detailed structures of individual star-forming regions and large-scale structures in the Galactic plane. The existing continuum surveys covering the first Galactic quadrant are, for example, the APEX Telescope Large Area Survey of the Galaxy at

870 μm (ATLASGAL; Schuller et al. 2009), the JCMT Galactic Plane Survey at 850 μm (JPS; Moore et al. 2015; Eden et al. 2017), the Bolocam Galactic Plane Survey at 1.1 mm (BGPS; Aguirre et al. 2011), the Herschel Infrared Galactic Plane Survey at 70–550 μm (Hi-GAL; Molinari et al. 2010), the Wide-field Infrared Survey Explorer survey at 3.4–22 μm (WISE; Wright et al. 2010), Spitzer's Galactic Legacy Infrared Mid-Plane Survey Extraordinaire at 3.6–8 μm (GLIMPSE; Benjamin et al. 2003; Churchwell et al. 2009), and MIPSGAL at 24 and 70 μm (Carey et al. 2009).

This paper presents the *full* COHRS data covering 52.8 deg^2, which is almost twice that of the first release, by completing the overall planned latitudes in a more extensive longitude range than the previous one. The R2 data are provided by mitigating the off-position contamination mentioned in Paper I and improving data reduction. In Section 2, we explain the COHRS observations and the general data reduction procedure. Section 3 provides information on the second release of the full COHRS data and how to access them online. Section 4 describes the noise characteristics. We present integrated position–position or position–velocity maps and descriptions of one-dimensional distributions in Section 5. Section 6 shows examples of COHRS data for three star-forming regions. In Section 7, we analyze the one-dimensional distribution of COHRS data and compare it with those of other data, such as the lowest ^{12}CO transition and star-forming populations. We summarize the main results in Section 8.

2. Observations and Data Reduction

2.1. Observations

COHRS is a spectral line survey mapping a strip of the Galactic plane in the first quadrant in the ^{12}CO (3–2) line (345.786 GHz). The survey covers a total of approximately 52.8 deg^2 in the region of $9°.5 \leqslant l \leqslant 62°.3$ and $|b| \leqslant 0°.5$. The observations were carried out with the Heterodyne Array Receiver Program (HARP; Buckle et al. 2009) on the 15 m James Clerk Maxwell Telescope (JCMT) in Hawaii.

The target longitude range for the original survey was $10° \leqslant l \leqslant 65°$. This was ultimately extended down to $l = 9°.5$ to follow the interesting structure seen in R1 around $l \sim 10°$. The upper end of the range was truncated to $l \sim 62°$; this decision was made in order to concentrate our remaining time on maximizing the overlap between COHRS and JPS, as well as on reobserving the noisiest tiles from R1. We chose not to reobserve those tiles affected by contamination in the off position. This decision was driven by time constraints and the desire to complete the survey area. We were confident that the effect of the contamination could be mitigated in postprocessing. We ultimately approached the issue of off-position signals by determining modal spectra and removing them during data reduction (see Section 2.2.1 for details).

The observations were taken over four semesters at the JCMT during 2013–2014 and 2017–2018. As in previous observations, the observing time was allocated as a mixture of PI time, which included some of CHIMPS2 time (proposal ID: M17BL004), Director's Discretionary Time, and empty-queue or poor-weather backup time (Panel for the Allocation of Telescope Time (PATT) Nos. M13AU41, M13BN02, and M14AU09). The data were collected in opacities ranging from $\tau_{225} \sim 0.06$ to $\tau_{225} \sim 0.31$. The observational strategies follow those described in Paper I.

---

[14] The Galactic region inside the solar circle is defined as the inner Galaxy.

HARP is a 4×4 array receiver with 16 superconductor–insulator–superconductor heterodyne detectors[15] arranged at intervals of $30''$. At the observing frequency, HARP has an angular resolution of $14''$ and a main-beam efficiency of $\eta_{mb} = 0.61$. The Auto-Correlation Spectral Imaging System (ACSIS; Buckle et al. 2009) was used as a setting for a 1 GHz bandwidth and 2048 frequency channels, providing a frequency resolution of 0.488 MHz or a velocity resolution of $0.42\,\mathrm{km\,s^{-1}}$. The bandwidth was set to a velocity coverage of $-400\,\mathrm{km\,s^{-1}} < v_{LSR} < +400\,\mathrm{km\,s^{-1}}$. The observations were taken in a position-switching raster (on-the-fly) mode with half-array spacing. The bulk of the off positions were measured above the Galactic plane with a latitude offset of $+2^\circ\!.5$.

2.2. Data Reduction

As with the original COHRS release, the observational data were reduced with the ORAC-DR pipeline software (Jenness & Economou 2015), specifically the REDUCE_SCIENCE_NARROWLINE recipe. This recipe invoked applications from the KAPPA (Currie & Berry 2013), SMURF (Chapin et al. 2013), and CUPID (Berry et al. 2007) packages, all from the Starlink collection (Currie et al. 2014). While the applications called by the recipe were from the Starlink 2018A release,[16] the ORAC-DR code included improvements made since that 2018A release[17] to address specific survey requirements. Jenness et al. (2015) provided a detailed description of the workings of the heterodyne recipes in ORAC-DR at the time of its writing.

Since the R1 data processing was finished, the reduction recipe has undergone many improvements, yielding better-quality products. Highlights include flat-fielding, masking of time intervals of spectra in Receptor[18] H07 affected by correlated noise called ringing (Jenness et al. 2015), and automated removal of emission from the reference (also called off-position) spectrum that appears as absorption lines in the reduced spectra, which can bias baseline subtraction and affect flux measurement of the emission. Since the removal of off-position signals was not written before Jenness et al. (2015), we describe the procedures that we adopted in Section 2.2.1.

Reductions were performed at least twice; the first automated attempt permitted visual inspection to assign values to recipe parameters, the most important being the baseline and flat-field regions, whether there were off-position signals or ringing spectra to remove. The recipe parameters used to control REDUCE_SCIENCE_NARROWLINE are available at the COHRS repository.[19] An annotated example parameter file is given in Appendix B.

In its quality assurance (QA) phase, the recipe used statistics to reject outlier spectra arising from nonastronomical sources, be it alternating bright and dark spectral channels or deviant baselines, both transient and persistent. The former typically rejected about 0.2% of the COHRS spectra. Due to ringing in Receptor H07 in about 5% of the observations, 5%–10% of the spectra therein were rejected. In about 65% of cases one to three entire receptors were expunged because of highly nonlinear baselines or overwhelming external noise sources.

A small number of observations were further excluded because they failed to meet QA thresholds, such as a maximum permitted T_{sys}. The QA parameters for COHRS are listed in Appendix A.

The second phase of the recipe converted the time-series spectra into PPV spectral cubes, grouping both components of the weave pattern (Buckle et al. 2009), and for some regions it incorporated data from multiple nights in order to yield a tolerable signal-to-noise ratio (S/N). The PPV cubes were regridded to $6''$ spatial pixels, and convolved with a $9''$ Gaussian beam, resulting in $16''\!.6$ resolution. The released data were also regridded along the velocity axis such that three raw channels became two channels, resulting in $\Delta V = 0.635\,\mathrm{km\,s^{-1}}$. As can be seen in Table 1, this higher resolution is more comparable to that of other surveys than the $\Delta V = 1.0\,\mathrm{km\,s^{-1}}$ of R1. This improvement will make structural analyses more effective. For example, the cloud catalog generated by Colombo et al. (2019) using the SCIMES catalog was limited in its ability to recover low-mass molecular clouds by the coarse velocity resolution. It also generates less channel-to-channel covariance than for a velocity width of an arbitrary round number.

In the second reduction run, only one iteration to refine baseline regions was necessary, aided by the chosen recipe parameters. R2 retained linear baseline fitting to avoid the creation of a small artificial dip across the emission regions excluded from the fitting process. Note that this contrasts with the fourth-order polynomial adopted by CHIMPS (Rigby et al. 2016). A first-order polynomial proved sufficient for the vast majority of COHRS observations.

Receptor-to-receptor responses were removed using a variant of the Curtis et al. (2010) summation method with user-defined velocity limits in which the median intensity approximately exceeded 0.2 K. In under 10% of observations, mostly for $l > 50^\circ$, there was insufficient signal to determine a reliable flat-field, the errors in the response ratios being comparable to or larger than those in the typical ratios themselves. Normalization was performed with respect to Receptor H05, except in the 14 cases where this receptor had failed QA, whereupon the reserve H10 became the reference receptor. On average H10 was 1.0% more sensitive than H05 for the COHRS data.

Mosaics of width 5° were formed from groups of PPV cubes with the PICARD (Gibb et al. 2013) recipe MOSAIC_JCMT_IMAGES in ORAC-DR. The recipe option chosen to perform the tiling itself was the WCSMOSAIC task from the KAPPA package. Spectral alignment was in the kinematic local standard of rest (LSRK).[20] It allocated pixel contributions using a Gaussian distribution with an FWHM of one pixel. The cube most central in each mosaic was assigned to be the reference for the world coordinate system, so as to minimize distortions in mapping from Galactic coordinates to a rectilinear pixel array. Then the tiles that form R2, which abut their neighbors, were extracted from the mosaics.

2.2.1. Correction of Off-position Signals

A significant deficiency with Release 1 was the presence of absorption features in 72% of the observations due to the

---

existence of emission in the off-position (also known as the reference) spectrum, itself still at relatively low Galactic latitudes. For Release 2 we have attempted to remove all detectable off-position features.

Previously, when circumstances made retrospective direct observations of the off position impossible, a common approach to dealing with a source in the reference position was to interpolate across the locations of such absorption. However, should these interpolated locations overlap a narrow emission line, the emission line could be erroneously weakened, or even eradicated. Likewise if the emission varied rapidly downward, mere interpolation may overcompensate for the reference signal. Since off-position features appear in every spectrum of an observation, we concluded that a better approach would be to determine the modal spectrum over regions devoid of emission or having minimal flux, then interpolate. Further, as receptors look at slightly different spatial locations, a modal spectrum should be derived for each receptor. The difference between each interpolated modal spectrum and the original modal spectrum derives an estimate of the reference signal for the corresponding receptor.

In outline, the off-position contamination mitigation operated as follows. For each receptor, the algorithm formed a pair of approximate reference spectra. The first of the pair was derived from the time-series cube where detected astronomical emission had been masked, whereas the other originated from the raw time series.

At first glance, using the emission-masked data ought to be sufficient, as it provides better discrimination between genuine dips arising from multiple-source emission at different velocities and those due to off-position absorption lines. In practice, however, incomplete detection of emission lines, due to noise dominating in the line wings, often left the off-position lines in steep-sided valleys, and as a result underestimated—typically by 0.1–0.2 K—the depth of these lines, and thus left residual absorption lines. In contrast the unmasked spectrum offered better estimates of the depth of reference spectral lines. However, the unmasked modal spectrum sometimes had difficulties discriminating between weaker source emission and a reference line with spectrally extended emission. The aim of using both modal spectra was to combine their assets: locate the lines with the masked version, and determine the line strengths from the unmasked version. Then the algorithm refined each of the approximate reference spectra to exclude source emission and background, to form an estimated reference spectrum.

Since the estimated reference spectrum should have a flat baseline at zero, accurate removal of the baseline is desirable. In practice this proved difficult in the presence of source emission, which might be extended and weak over a wide velocity range. Our algorithm took an iterative approach of twice measuring and masking lines from the off position and then from sources. The line masking yielded better estimates of the background signal, which after subtraction led to better estimates of the line strengths, and to an improved baseline. The derived reference spectrum was subtracted from every spectrum in the time-series cube. Details of the automated algorithm are provided in Appendix C.

The automated algorithm left no perceptible absorption feature for about a third of the lines, but over half of the lines were only partially corrected, mostly caused by the noise raising the subtracted base level, thus not quite removing all of the reference line. A typical residual was 0.04 K. The method was also less reliable for reference lines located where there was varying and much broader source emission. In about a tenth of cases the reference line was not removed at all or a prominent line was left, albeit one that was much weaker, but still could be several tenths of a kelvin deep in the most extreme cases.

For cases where reference lines were still present after the automated filtering, an additional processing step was performed. This required the velocity limits of the residual reference lines to be supplied via a recipe parameter. First, these line regions were masked in the modal spectra for each receptor. Then a smooth function based on iterative approximate solutions to Laplace's equation filled the gaps. The difference between the interpolated and original spectra then yielded estimates of the residual reference line.

Despite this further attempt, off-position lines stubbornly remained in seven observed sections of the survey. The cause was the presence of a sheet of emission at the velocity of each absorption line, where the sheet spanned the bulk of the spatial pixels. As a consequence, the median or modal spectrum was representative of the emission, rather than being near or at the baseline.

To circumvent this obstacle, for each survey section we manually extracted a polygonal spatial area devoid of emission at the line velocity. For each area we computed the median spectrum. This was smoothed with a Gaussian kernel with an FWHM of 25 channels to determine the residual baseline. The smoothing was barely affected by the off-position lines that only spanned a few channels. Subtraction of the smoothed spectrum from the original median spectrum resulted in a flat baseline at zero. However, in four cases, where the off-position line was located in strong emission, a small offset (ranging from 0.003 to 0.03 K) correction was applied to bring the neighboring baseline to zero. Spectral channels beyond the off-position absorption line were set to zero. The name of this estimated reference spectrum was passed to REDUCE_SCIENCE_NARROWLINE through a recipe parameter, so that it could be added to the reference spectrum formed by the previous method when the observations were reduced again.

We performed sanity checks of our off-position corrections by comparing the median spectra of the same overlapping regions of adjacent observations. In order to compare like with like, undefined spectra in either observation were masked in both regions, and the spectra were aligned along the spectral axis. Each overlap region typically contained 20,000 spectra. Besides giving confidence in the existing corrections, these revealed many weak off-position signatures, as evidenced by similar dips in one observation compared with all of its neighbors. For some overlaps, both neighbors exhibited a colocated residual absorption feature, and thus the procedure required a few iterations. This was particularly evident for $l = 22°$–33°, where the Aquila Rift gave rise to a common $8 \mathrm{~km~s}^{-1}$ off-position line spanning a sequence of regions. These were corrected in 72 cases by using the second semiautomated method described earlier, usually with adjustments to the previously estimated line bounds. If that failed wholly or partially, the manual approach was adopted (in 59 cases). For this final resort variance-weighted average displacements from the neighboring median spectra within the velocity limits of the off-position signal were used to form a spectrum to be subtracted.
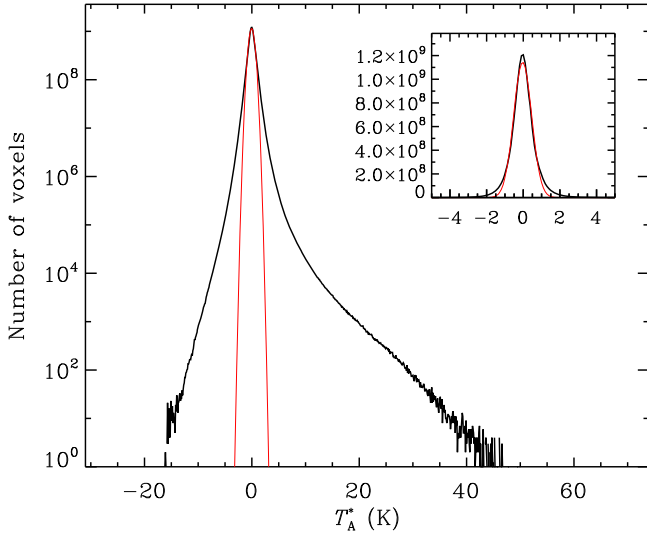
Figure 1. Histogram of the corrected antenna temperature for all voxels in COHRS, displayed on a logarithmic scale. The bin width is 0.1 K. The red curve shows a Gaussian fit to the distribution described by $1.14 \times 10^9 \exp\left(-\frac{1}{2}(T_A^* - 0.032)^2 / 0.49^2\right)$. The inset shows the same distribution on a linear scale.

3. Data Release 2

We provide 106 tiles in FITS format with a $0°\!.5$ longitude width and a full latitude range ($0°\!.5 \times 1°\!.0$ per one tile). All of them are perfectly contiguous. Each tile is named in the form of central Galactic coordinate values and suffixes indicating the nature of the file, e.g., COHRS_09p50_0p00. Exceptionally, the first tile with the string "09p50" in its name is in the range of $l = 9°\!.5$ to $9°\!.75$ with a longitudinal width of $0°\!.25$. All intensities are in units of T_A^*. The corrected antenna temperatures T_A^* can be converted to main-beam brightness temperatures T_{mb} by dividing them by $\eta_{mb} = 0.61$. Along the velocity axis, the data cubes in the second release have been cropped to a range of $-200\,\mathrm{km\,s^{-1}} < v_{LSR} < +300\,\mathrm{km\,s^{-1}}$, which is extended as compared with that of the first release ($-30\,\mathrm{km\,s^{-1}} < v_{LSR} < +155\,\mathrm{km\,s^{-1}}$). The R2 data cubes can be obtained online from the CANFAR data archive (Gaudet et al. 2009), publicly accessible at doi:10.11570/22.0078. We note that comparison plots for R1 and R2 are also stored in the same archive.

Figure 1 shows a histogram of the corrected antenna temperature (T_A^*) for all voxels. The values can be modeled as a normal distribution with a mean value of 0.036 K and a standard deviation of 0.49 K. The distribution shows a strong positive tail and a relatively weak negative tail. While the former is primarily due to voxels containing $^{12}\mathrm{CO}\,(3\text{--}2)$ emission, the latter is significantly affected by random noise fluctuations in voxels with much-higher-than-average noise levels (e.g., many of them are at $|b| \gtrsim 0°\!.3$). The tile name and the mean rms noise for each tile are tabulated in Table D1 of Appendix D.

4. Noise Characterization

A histogram and two-dimensional map of the rms noise levels of the spectra across the COHRS areas are shown in Figures 2 and 3, respectively. The noise levels were measured by taking the standard deviation of the baseline over a velocity range, $v_{LSR} < -100\,\mathrm{km\,s^{-1}}$ or $v_{LSR} > +200\,\mathrm{km\,s^{-1}}$, in which no astronomical signal was visible. The histogram peaks at
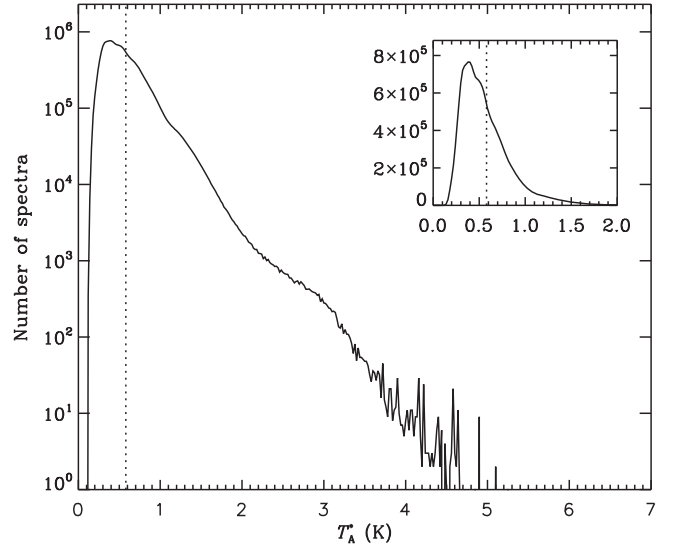

Figure 2. Histogram of the noise for all pixels in COHRS, displayed on a logarithmic scale. The bin width is 0.02 K. A dotted vertical line indicates the mean value of noise levels across the survey. The inset shows the same data on a linear scale.

about 0.3 K, close to the standard deviation of the normal distribution of all voxels shown in Figure 1, and contains a fat tail, mainly contributed from the noisiest areas at relatively high latitudes (see Figure 3). The variation across the noise map results from the combined effect of weather conditions, observing elevations, and the number of HARP receptors included in the reduction. We found that 27% of the pixels have rms noise levels $<0.4\,\mathrm{K}$, 60% have levels $<0.6\,\mathrm{K}$, and 80% have levels $<0.8\,\mathrm{K}$. The mean and median values of the noise levels are 0.6 K and 0.5 K, respectively. Figure 4 shows a histogram of the S/N for all voxels indicating the noise is Gaussian (normal distribution). The positive tails in the log plot are due to real astronomical signals.

The average of the rms noise values of all pixels for each tile is given in Table D1 of Appendix D. For tiles with the full latitude range of R1 shown in Table 3 of Paper I, their rms noise level in R2 is reduced to 13%–55% (36% on average). As mentioned in Paper I, some of the final tiles contain maps observed on different nights and under different conditions, resulting in some significant changes in rms noise levels in one tile. Therefore, in such a case, it is not appropriate to say that the average rms is a representative value for an individual map. Instead, Figure 3 is helpful for visualizing the spatial noise distribution throughout the survey and within each tile.

5. Results

5.1. Integrated Position–Position Maps

Figure 5 shows channel maps of $^{12}\mathrm{CO}\,(3\text{--}2)$ emission with a velocity interval of $20\,\mathrm{km\,s^{-1}}$ from $v_{LSR} = -50$ to $150\,\mathrm{km\,s^{-1}}$ as well as an integrated map over the whole velocity range.

Most of the $^{12}\mathrm{CO}\,(3\text{--}2)$ emission in the ranges of $l \simeq 10°$ to $22°$ and $38°$ to $45°$ appears in negative latitudes. Such a tendency between $l = 12°$ and $22°$ was reported by Umemoto et al. (2017) using the FUGIN $^{12}\mathrm{CO}/^{13}\mathrm{CO}/\mathrm{C}^{18}\mathrm{O}\,(1\text{--}0)$ maps. They explained that this is a distance effect that occurs because the Sun is not located at the true Galactic midplane. The Sun is located slightly above the true Galactic midplane, and an estimated offset is $\sim$10–30 pc (e.g., Karim & Mamajek 2017;
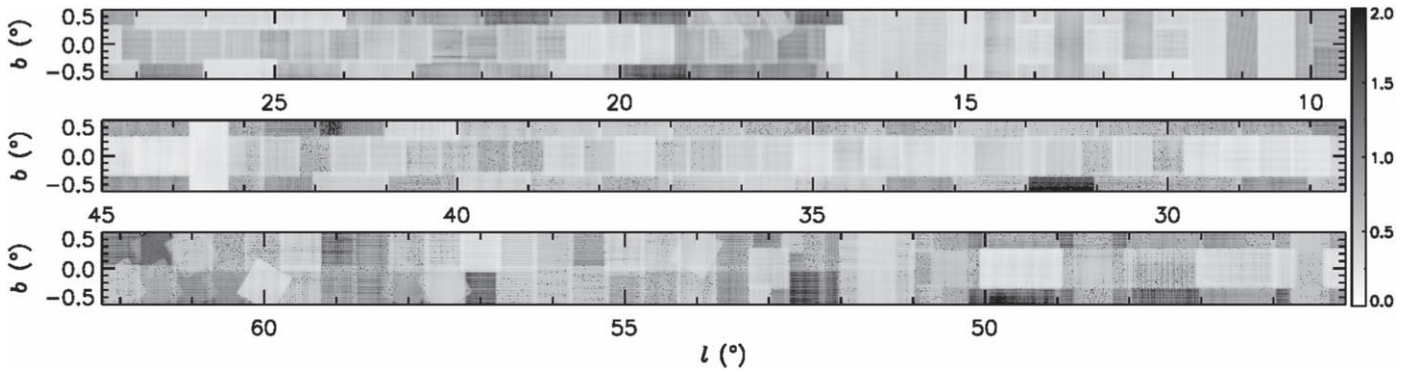
Figure 3. Noise maps for the COHRS data. The noise level was obtained by the conventional way, which calculates rms values over velocity ranges where there is no astronomical signal (see text for details). The intensity scale is in T_A^* (K).
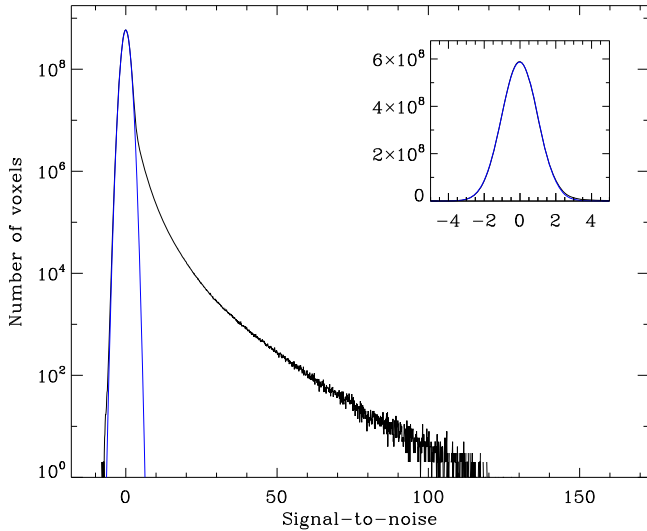

Figure 4. Histogram of the S/N for all voxels in COHRS, displayed on a logarithmic scale. The bin width is 0.1 K. The blue curve is a Gaussian with a width (standard deviation) of 1 centered at 0. The inset shows the same distribution on a linear scale.

Anderson et al. 2019, and references therein). Many previous studies to estimate the Sun's height used the star count method. Recent studies by Su et al. (2016, 2019) used a large-scale CO gas distribution to derive the position of the Sun, yielding ~17 pc, which is similar to the median of the published estimates. For objects located at the true Galactic midplane, those closer to the Sun will appear at higher negative latitudes while those at a larger distance will converge to $b = 0°$. On the other hand, the remaining $^{12}CO\,(3-2)$ emission regions are roughly distributed around $b = 0°$. But we note that positive-velocity channels contain $^{12}CO\,(3-2)$ components at two distances along the line of sight, the near and far. Therefore, $^{12}CO\,(3-2)$ emissions originating from two very different distance ranges are stacked up, and the distance effect of this discrepancy for each line of sight should be carefully considered.

Many prominent bright regions appear across the COHRS area while significant faint extended emission is detected. Some of the bright regions include well-known star-forming regions, such as W31 ($l = 10°3$), W33 ($12°8$), W42 ($25°3$), W43 ($30°8$), W47 ($37°6$), W49A ($43°2$), and W51 ($49°4$). Among them, three massive and luminous star-forming regions, W43, W49A, and W51, are presented in Section 6.

5.2. Integrated Position–Velocity Map

A position–velocity (l–v_{LSR}) map of $^{12}CO\,(3-2)$ emission integrated over the whole latitude range is shown in the top panel of Figure 6. The bottom panel presents the same $^{12}CO\,(3-2)$ l–v_{LSR} map, but with known H II regions and spiral arm loci overlaid. The H II regions were obtained from version 2.2 of the all-sky WISE catalog (Anderson et al. 2014) as hosted by IRSA (Anderson et al. 2020). Note that the H II regions shown here are those given a single measured velocity, but the original WISE catalog lists numerous H II regions with no available velocity measurement or many H II regions with multiple velocities measured. The traces of spiral arms were derived from Reid et al. (2016) and updated in Reid et al. (2019). In the figure, the main spiral arms (Scutum Arm, Sagittarius Arm, Perseus Arm, and Norma-Outer Arm) and interarm features (Local Spur, Aquila Spur, Aquila Rift, and 3 kpc Arm) are drawn. $^{12}CO\,(3-2)$ emission, in general, agrees well with the spiral-arm traces although those associated with the Outer Arm are extremely faint and sparsely distributed. The Aquila Rift ranges from about $17°$ to $43°$, from which bright parts near $l = 18°$–$22°$ and $32°$–$36°$ are clearly seen. Also, in the remaining sections, weak $^{12}CO\,(3-2)$ emission appears along locations where other CO isotopologue emissions are detected (see Figure 5 of Dame & Thaddeus 1985 and Figure 3 of Jackson et al. 2006). Well-studied star-forming regions such as W43 (l, $v_{LSR} = 30°9$, $95\,km\,s^{-1}$) and W51 ($49°4$, $60\,km\,s^{-1}$) show highly peaked emission with complex velocity structures. The locations of H II regions generally coincide with CO-bright regions. This characteristic is illustrated by comparing the probability distribution functions (PDFs) for the entire $^{12}CO\,(3-2)$ distribution and the $^{12}CO\,(3-2)$ distribution related to the H II regions (see Figure 7). We extracted the H II region–related $^{12}CO\,(3-2)$ from the (d_{HII}, d_{HII}, 15) pixel bin at each H II region location. The variable d_{HII} is the diameter of the H II region given in the WISE catalog, and 15 pixels at velocity were arbitrarily chosen to have about $10\,km\,s^{-1}$. The PDF of H II region–related $^{12}CO\,(3-2)$ has a lower peak, which is mainly contributed by noise, and a fatter positive tail, which indicates stronger CO signals, compared to the PDF of all $^{12}CO\,(3-2)$.

6. Example COHRS Data

Examples of COHRS data for active star-forming regions, such as W43, W49A, and W51, are displayed in Figures 8–10. These figures present integrated-intensity maps from two rotational transitions of two CO isotopologues ($^{12}CO/^{13}CO$
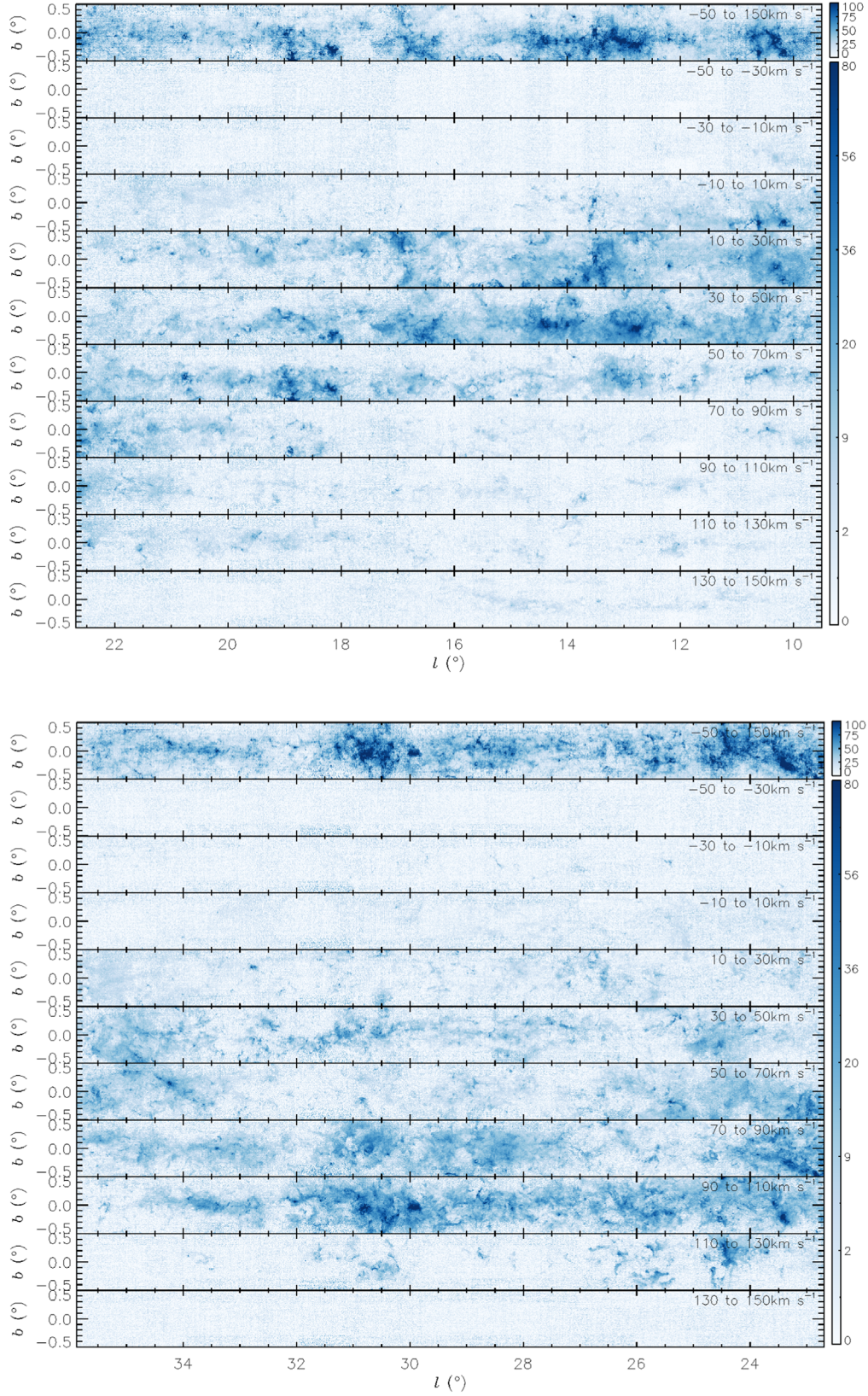
Figure 5. The maps of velocity-integrated emission (T_A^*) in COHRS. These maps were obtained by integrating over the velocity range written at the top of each panel. The units on the intensity scale are K km s^{-1}.

(1–0) and (3–2)) from FUGIN, COHRS, and CHIMPS data together with 8 μm (GLIMPSE I; GLIMPSE Team 2020) and 850 μm (JPS or Eden et al. 2018) continuum maps, if available. Also, examples of available CO spectral lines obtained from the nearest position to the velocity-integrated ^{12}CO (3–2) emission peak are shown. That is, spectra of different CO isotopologues and transitions were extracted from the matching positions within the one-pixel size of each survey. The COHRS
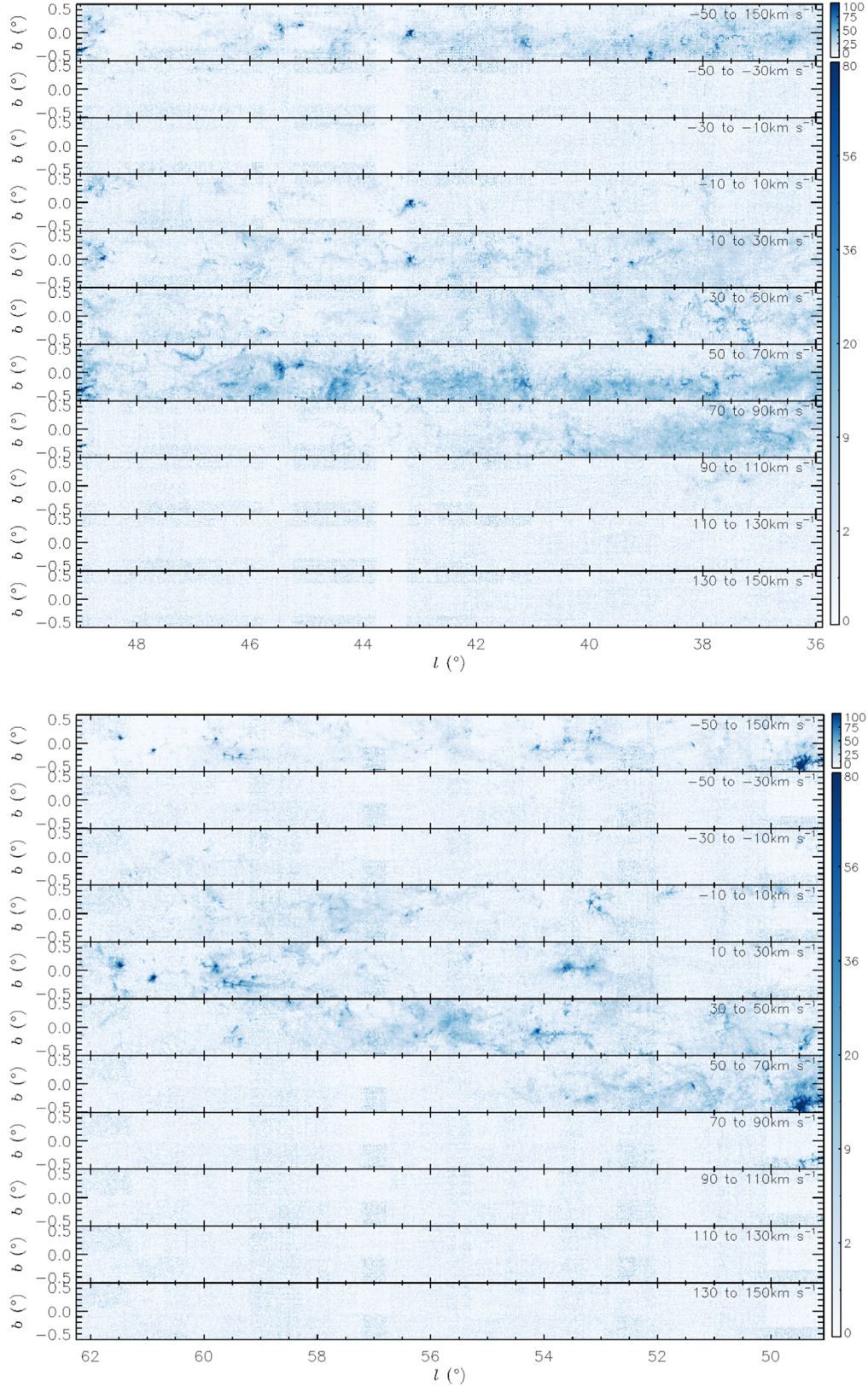
Figure 5. (Continued.)

emission maps show clearly the clumpy or filamentary structures and in addition extended diffuse CO gas as compared with other CO maps. Also, the bright clumpy or filamentary features appear to be closely associated with star-forming regions seen in the continuum maps.

W43 is one of the most massive molecular complexes (total gas mass ($M_{\rm gas}$) of $\sim 7.1 \times 10^7\,M_\odot$, bolometric luminosity ($L_{\rm bol}$) of $\sim 8.5 \times 10^5\,L_\odot$; Nguyen Luong et al. 2011; Urquhart et al. 2014b) in the Galaxy. The distance of W43 is estimated to be 5.5 kpc from the Sun (Zhang et al. 2014). The region is
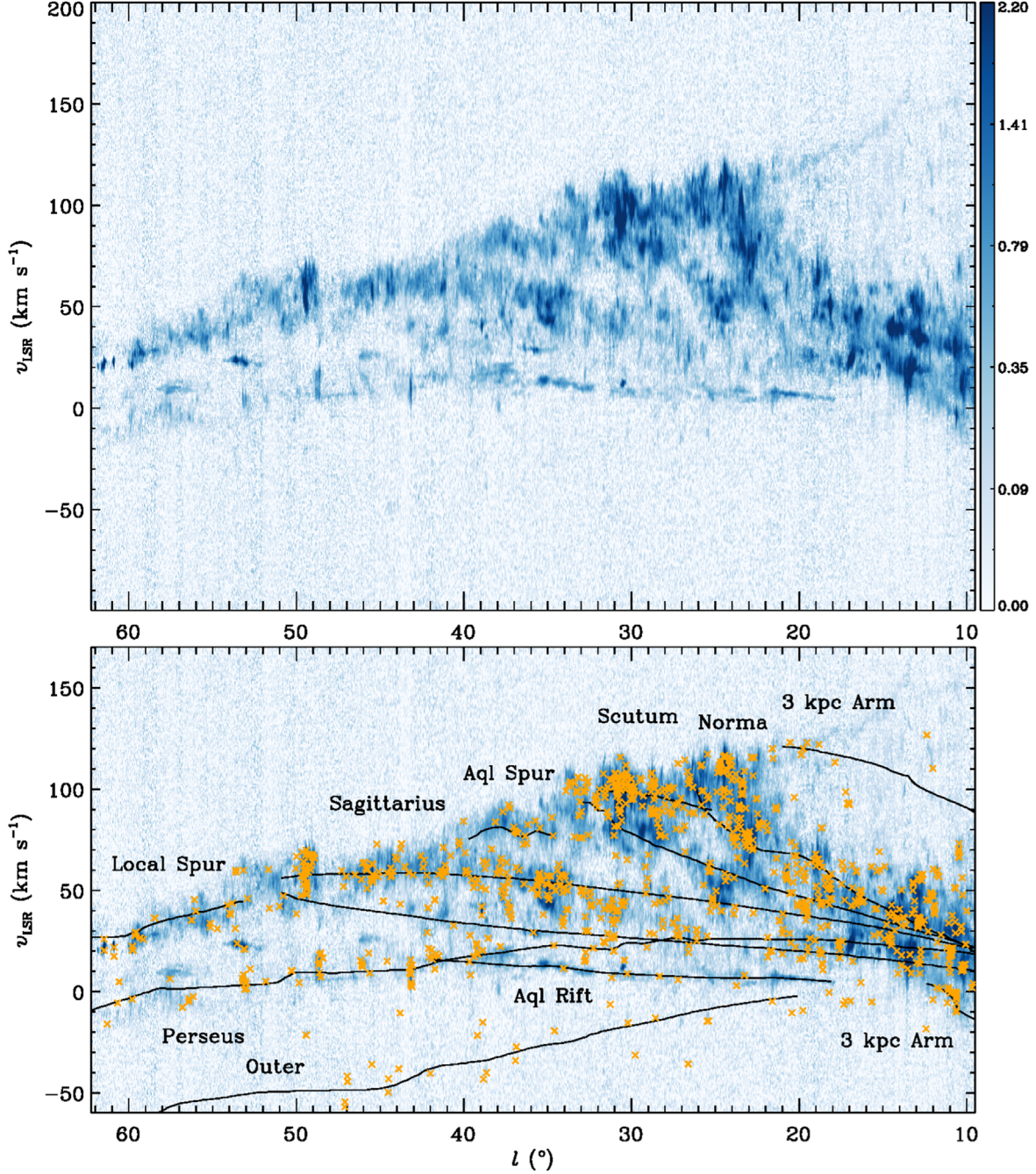
Figure 6. Position–velocity (l–v_{LSR}) map for the ^{12}CO (3–2) emission (T_{mb}) in COHRS. This map was obtained by integrating over the latitude axis. The map is drawn on a square-root scale. The units on the intensity scale are K degrees. The bottom image is the same as the top, but is shown for a narrower velocity range overlaid with known H II regions and spiral arm loci. Cross symbols indicate WISE H II regions. The traces of the main spiral arms (Scutum Arm, Sagittarius Arm, Perseus Arm, and Norma-Outer Arm) and interarm features (Local Spur, Aquila Spur, Aquila Rift, and 3 kpc Arm) from Reid et al. (2016, 2019) are overlaid using black curves.

located near the tangential point of the Scutum Arm, where the spiral arm meets the Galactic bar (Nguyen Luong et al. 2011). It appears between $l = 29°$ and $32°$ and between $b = -1°$ and $+1°$ in the velocity range $v_{LSR} = 80$–$110\,\mathrm{km\,s^{-1}}$ (e.g., Nguyen Luong et al. 2011; Kohno et al. 2021). W43 extends beyond the latitude coverage of COHRS, but the brightest parts such as W43-main ($l \sim 30°8$) and W43-south ($l \sim 29°9$), which are very active star-forming regions, are covered, as seen in Figure 8. W43-main is considered as a ministarburst region, which contains 51 protocluster candidates (Motte et al. 2003). Kohno et al. (2021) suggested that a supersonic cloud–cloud collision causes the local ministarbursts in W43.

W49A is another one of the most well-known massive and luminous Galactic star-forming complexes ($M_{gas} \sim 1.1 \times 10^6 \, M_\odot$, $L_{bol} \sim 3.63 \times 10^6 \, L_\odot$; Galvan-Madrid et al. 2013; Urquhart et al. 2014b), despite being located at a large distance of 11.1 kpc from the Sun (Zhang et al. 2013). It is centered at (l, b) = ($43°15$, $-0°01$) and appears in the LSR velocity range of -20 to $+30\,\mathrm{km\,s^{-1}}$. The region lies on the Perseus Arm in the inner Galaxy. The GMC of W49A extends more than 100 pc ($\sim30'$) in longitude (Simon et al. 2001), while active star formation occurs mainly in the central area within ~20 pc ($\sim6'$) (Welch et al. 1987; Alves & Homeier 2003). As shown in Figure 9, the bright CO emission region is aligned along the line of sight with the
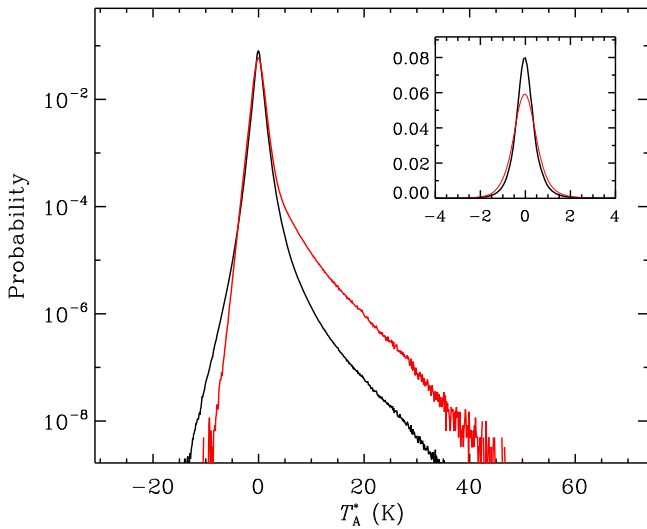
Figure 7. Temperature PDFs of the entire ^{12}CO (3–2) distribution (black) and the H II region–related ^{12}CO (3–2) distribution (red) in COHRS.

central star-forming region, and the CO maps show clear hub–filament structures (Galvan-Madrid et al. 2013). A ring- or shell-shaped, faint CO emission feature extends westward from the central bright region. The extended feature is visible in ^{12}CO (1–0), but clearer in ^{12}CO (3–2). Much weaker and clumpier ^{13}CO emission features are discernible where the structure shown in the ^{12}CO maps is located. The ^{12}CO profiles in Figure 8 show a double-peak feature due to self-absorption at $v_{LSR} \sim 7$ km s^{-1}, which is stronger in the (1–0) line than in the (3–2) line. On the other hand, the two transitions of ^{13}CO have different velocity profiles, indicating that the two transitions trace different internal conditions.

W51 is also a particularly prominent massive and luminous Galactic star-forming complex ($M_{gas} \sim 1.2 \times 10^6 \, M_\odot$, $L_{bol} \sim 4.68 \times 10^6 \, L_\odot$; Carpenter & Sanders 1998; Urquhart et al. 2014b). It is estimated to be at a distance of 5.4 kpc from the Sun (Sato et al. 2010) and is located near the tangent point of the Sagittarius Arm. The region is centered on $(l, b) \approx (49°.4, -0°.3)$, and appears as a long filamentary stream with a length of ~ 100 pc, which is mostly covered by COHRS data (see Figure 10). The W51 GMC is distributed in a broad velocity range of $v_{LSR} = 30–85$ km s^{-1} (Kang et al. 2010), and embeds two star-forming regions, W51A and W51B, and hosts a supernova remnant W51C. The brightest region of CO emission near $(l, b) \approx (49°.5, -0°.4)$ shown in Figure 10 is associated with W51A. The ^{12}CO profiles show a clear double peak due to self-absorption around $v_{LSR} = 65$ km s^{-1}. The self-absorption feature is stronger in (3–2) than in (1–0), indicating the foreground gas is likely colder than the gas associated with the W51 complex. However, the self-absorption situation can occur in subthermal excitation, where the density is lower than the effective critical density, even if the gas is not colder. Therefore, additional analysis is needed to understand the actual situation.

7. Comparison with Other Data: One-dimensional Distributions

7.1. ^{12}CO (1–0) versus ^{12}CO (3–2)

The FUGIN survey mapped part of the first quadrant of the Galactic plane at the lowest rotational transition (1–0) of three CO isotopologues (^{12}CO/^{13}CO/C^{18}O) with an angular resolution comparable to that of COHRS (see also Table 1 for

detailed survey information). ^{12}CO (1–0) is a fundamental rotation transition expected to be excited even in the coldest and most diffuse molecular ISM. Its critical density at 10 K is $\sim 10^3$ cm^{-3} while that of ^{12}CO (3–2) is $\sim 10^4$ cm^{-3}. However, for ^{12}CO, radiative trapping causes the molecule to emit at a density an order of magnitude lower than its critical density. In any case, the (3–2) emission line is emitted in relatively warmer and denser ISM conditions than (1–0).

Figure 11 presents the longitudinal (l), latitudinal (b), and velocity (v_{LSR}) distributions of normalized integrated intensity for COHRS ^{12}CO (3–2) (blue profiles) and FUGIN ^{12}CO (1–0) (black profiles). Each profile was obtained by integrating over the two orthogonal axes, and then the intensity was normalized to the peak intensity in the profile. Note that FUGIN was mapped over a more limited longitudinal range ($l \leqslant 50°$) than COHRS. Since intensity variations along longitudes were much larger than the pixel size of the survey data ($6''$ for COHRS and $8''.5$ for FUGIN), the original l-profiles were smoothed to have a bin size of $60''$ using the IDL INTERPOL function to provide better visual exhibition. On the other hand, the b- and v_{LSR}-profiles are displayed without smoothing. Periodic oscillations in the FUGIN b-profile exhibit a horizontal stripe pattern caused by instrumental artifacts.

Both l-profiles integrated over latitude and velocity for the two transitions tend to decrease in general above $l = 30°$. This is because the distribution of the molecular ISM is not uniform in the Galactic disk and the Sun is far from the Galactic center. First, most of the molecular ISM is concentrated in the inner Galactic disk, and the distance (Δd_{los}) from the Sun and the far side of the inner disk steeply decreases with increasing longitude ($\Delta d_{los} \sim 6$ kpc for two lines of sight, $l = 60°$ and $30°$, while $\Delta d_{los} \sim 2$ kpc for two lines of sight, $l = 30°$ and $10°$). In other words, more CO emission lines usually accumulate along the line of sight toward lower Galactic longitudes. Second, the molecular ISM is strongly associated with the Galactic spiral arms and the arrangement of the spiral arms along the line of sight affects the shape of the l-profiles (see Figure 6 for an example). Above $l = 30°$, there are fewer spiral arms lying close to the Sun. On the other hand, l-profiles with $l < 30°$ show large fluctuations rather than a smooth change in profile strength. This is mainly caused by how many luminous velocity components (or GMCs) overlap in a line of sight. Between the two transition profiles, the peak locations are generally equal to each other. The strengths of the two profiles are also similar in some longitudes (for example, at $l \sim 30°.5$ and $35°$), but their distinction is clearly seen in many other longitudes. While (3–2) emission becomes more strongly peaked than (1–0) emission, for example, at $l \sim 13°$, $23°.5$, $24°.5$, $43°$, and $49°.5$, the predominance of (1–0) emission appears mainly at weak peaks or between peaks. The three prominent star-forming regions mentioned in Section 6 are also well located at CO peaks. The comparison with such star-forming populations will be discussed in the next section.

The b-profiles integrated across longitude and velocity for the two CO transitions have a shape close to a normal distribution since lots of components of CO emission are integrated over a wide (l, v_{LSR}) range. Least-squares Gaussian fitting gives best-fit functions of $0.940 \exp\left(-\frac{1}{2}(b - 0.115)^2 / 0.428^2\right)$ and $0.948 \exp\left(-\frac{1}{2}(b - 0.105)^2 / 0.365^2\right)$ for (1–0) and (3–2), respectively. They have nearly equal peak positions and a slightly stronger negative wing than a positive one, but the normalized intensity of the (3–2) profile decreases more rapidly than that of the (1–0) profile.
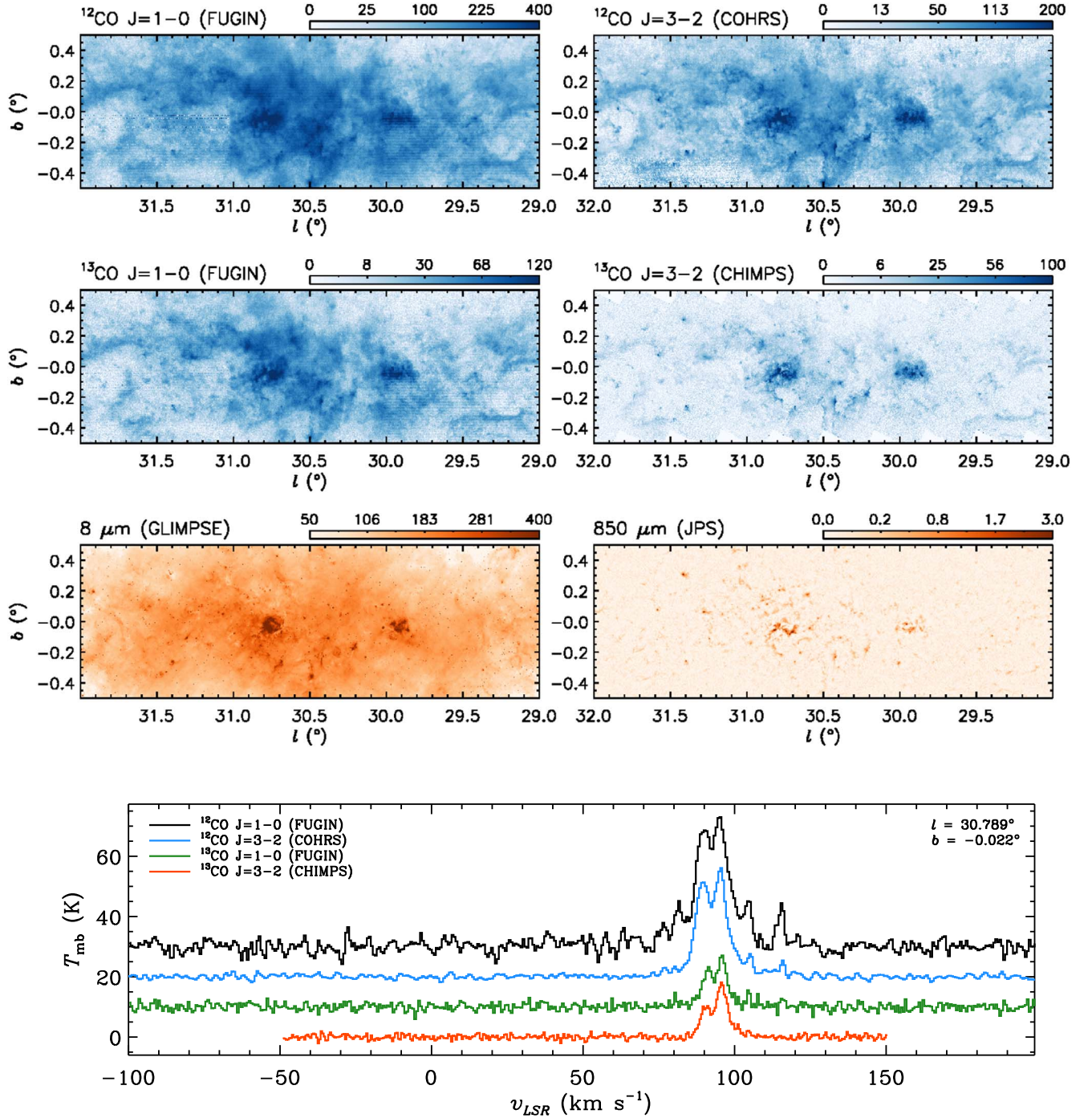
Figure 8. W43 star-forming region within the COHRS coverage area. From the top left to the bottom, each panel displays ^{12}CO (1–0) FUGIN data, ^{12}CO (3–2) COHRS data, ^{13}CO (1–0) FUGIN data, ^{13}CO (3–2) CHIMPS data, 8 μm GLIMPSE data, 850 μm JPS data, and examples of CO spectra, respectively. The CO maps are velocity-integrated over the v_{LSR} range of (80, 110) km s^{-1} (Nguyen Luong et al. 2011), and the units on the intensity scale of the integrated main-beam temperature are K km s^{-1}. The units on the intensity scale of the GLIMPSE and JPS data are MJy sr^{-1} and Jy beam^{-1}, respectively. The CO spectra were obtained at the position closest to the velocity-integrated ^{12}CO (3–2) emission peak. The offsets of 10 K, 20 K, and 30 K to the spectra have been added for better visualization.

7.2. ^{12}CO Emission versus Star-forming Population

As shown in the l- and b-profiles, the v_{LSR}-profiles integrated over longitude and latitude for the two transitions look similar to each other. In other words, the peak positions of the two profiles, each normalized by its maximum intensity, are almost the same. However, except for the two peaks at $v_{LSR} \sim 50$–60 km s^{-1}, (1–0) emission is always stronger than (3–2) emission. The difference is relatively more pronounced at $v_{LSR} \sim 5$–15 km s^{-1}, indicating the presence of more diffuse local emission in (1–0).

The detection of H II regions is the clearest evidence for ongoing massive star formation. The WISE catalog provides the entire-sky Galactic H II regions identified using mid-infrared data. In the area where COHRS and FUGIN overlap ($l = 10°$–50° and $b \leqslant 0°.5$), we found 2179 WISE H II regions, excluding one source with no radio data. On the other hand, as the densest parts within GMCs are where star formation can take place, dense molecular clumps can be at various early
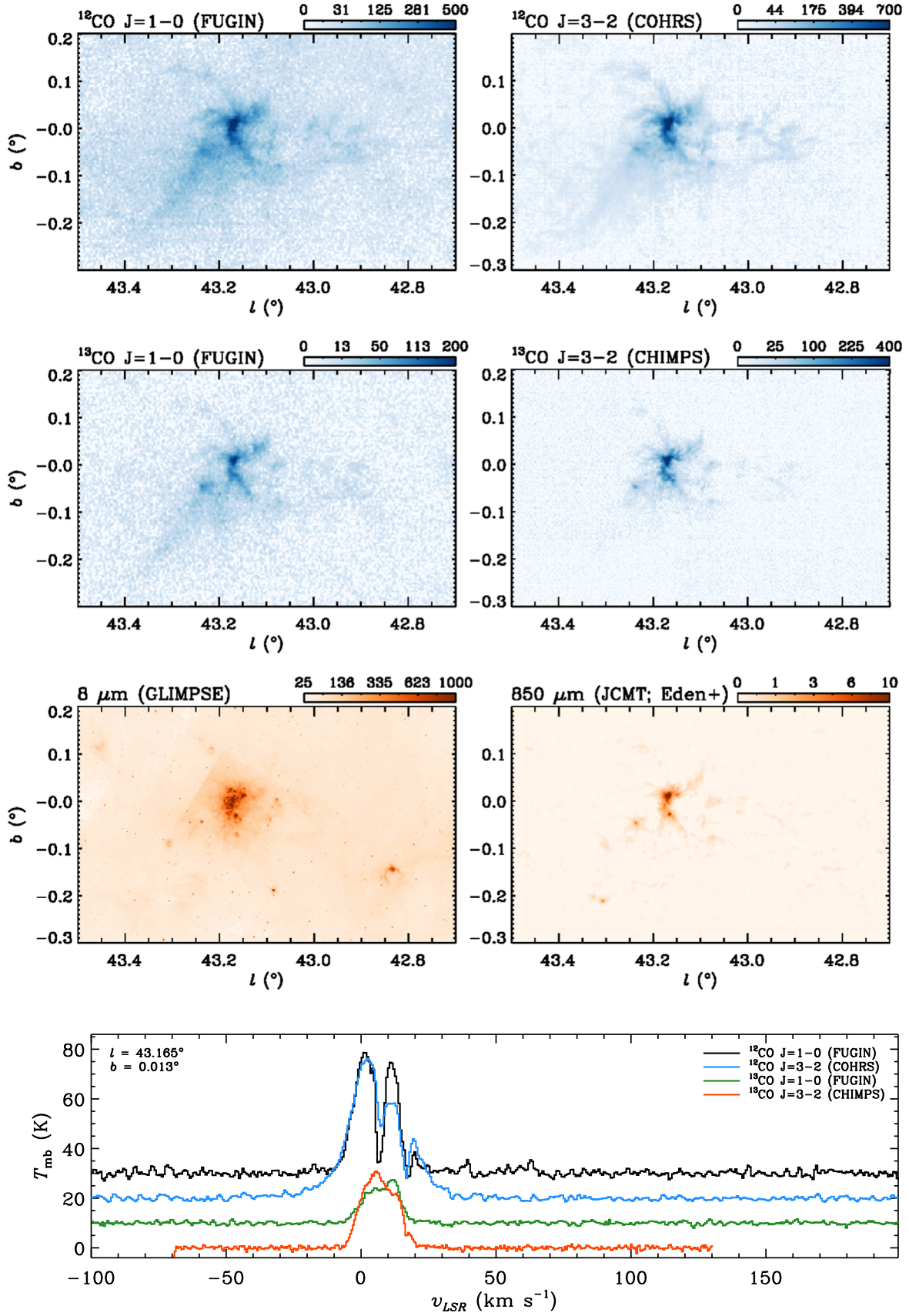
Figure 9. Same as Figure 8, but for the W49A star-forming region. The 850 μm continuum data were taken from Eden et al. (2018). The CO maps are velocity-integrated over the v_{LSR} range of $(-20, +30)$ km s^{-1} (Galvan-Madrid et al. 2013). In the GLIMPSE 8 μm image, instrumental artifacts remain around the bright W49 area at $(l, b) \sim (43^\circ.17, -0^\circ.01)$.
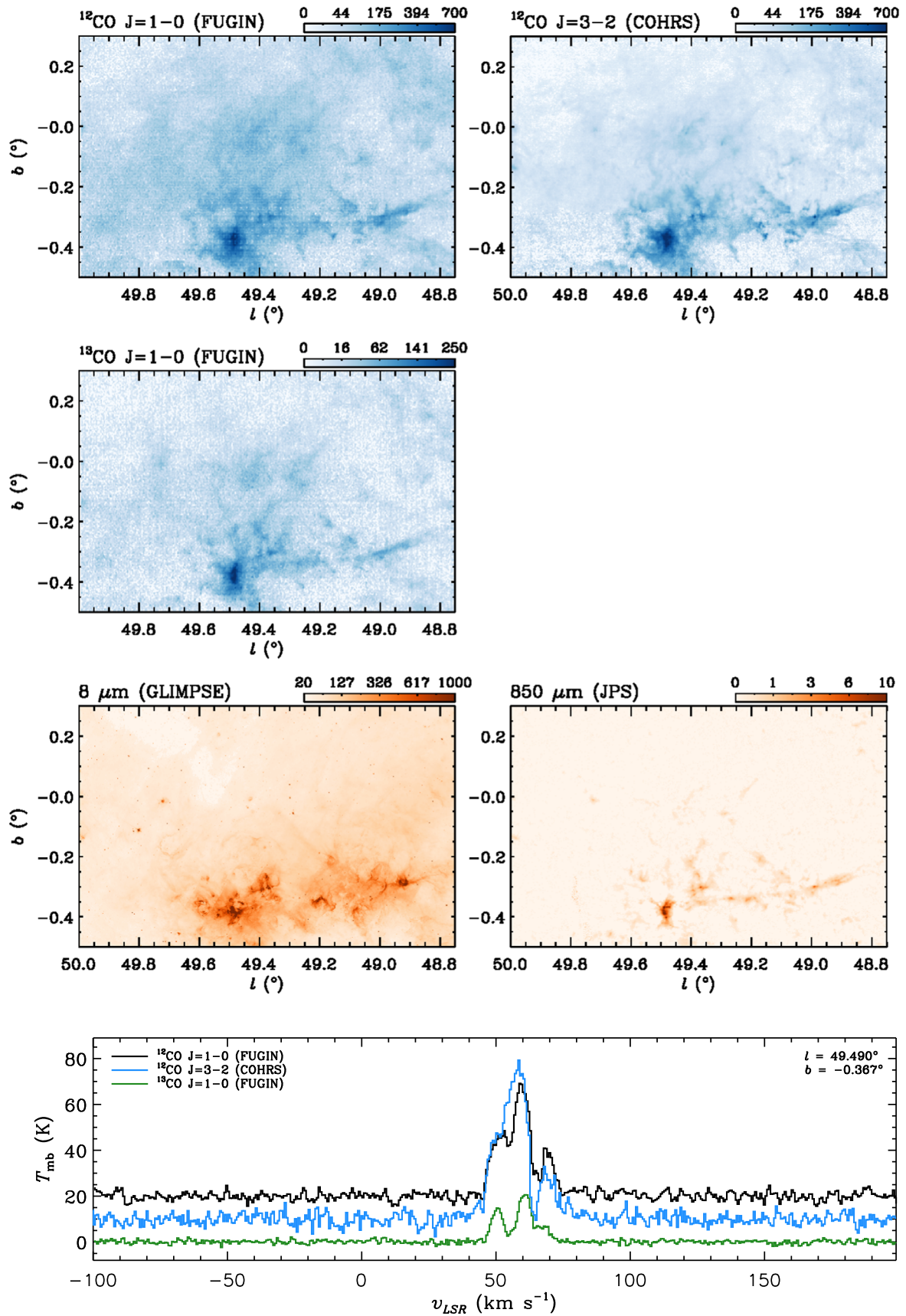
Figure 10. Same as Figure 8, but for the W51 star-forming region. The CO maps are velocity-integrated over the v_{LSR} range of (30, 85) km s^{-1} (Kang et al. 2010). There are no available CHIMPS data for this region.
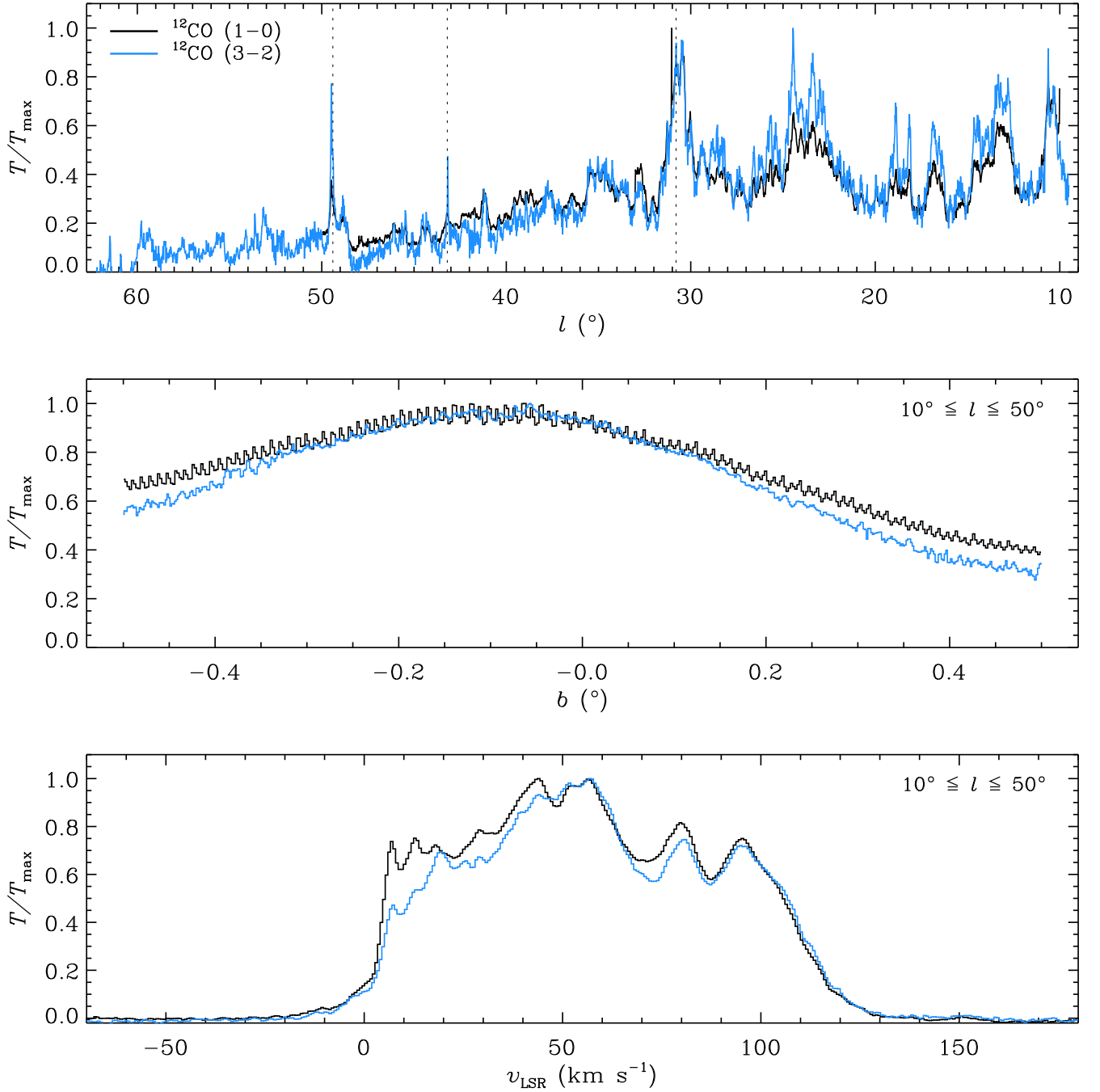
Figure 11. Integrated (one-dimensional) l, b, and v_{LSR} distributions of ^{12}CO (1–0) (FUGIN; black) and ^{12}CO (3–2) (COHRS; blue). Each profile was obtained by integrating across the two orthogonal axes. Note that the b- and v-profiles are restricted to data within $10° \leqq l \leqq 50°$ since available FUGIN data are limited to that Galactic longitudinal range. CO intensity was normalized to the peak value of each profile. The two CO l-profiles were smoothed to have a bin size of $\sim60''$, while the b- and v-profiles have a bin size corresponding to the latitudinal pixel size and velocity channel width of each CO data cube, respectively. On the top panel, three vertical dotted lines are drawn to help locate three star-forming regions: W43 ($l = 30°.8$), W49A ($43°.2$), and W51 ($49°.4$).

evolutionary stages of star formation, from the starless to the early embedded stages. The ATLASGAL compact-source catalog provides about 10,000 dense clumps in the range of $|l| < 60°$ and $|b| < 1°.5$ (Contreras et al. 2013; Urquhart et al. 2014a) found by using submillimeter survey data. For about 8000 of these dense clumps in $5° < |l| < 60°$, Urquhart et al. (2018) investigated the detailed properties including velocities, distances, luminosities, masses, and inferred evolutionary stages using mid- and far-infrared survey data. Their classification scheme divides clumps into four groups: massive star–forming (MSF) clumps, young stellar object (YSO)–forming

clumps, protostellar clumps, and starless or pre-stellar clumps. In the area where COHRS and FUGIN overlap, 2178 ATLASGAL clumps with signs of star formation (i.e., excluding those that are classified to be in the quiescent phase or are unclassified) were identified, including 455 MSF clumps, 1222 YSO-forming clumps, and 501 protostellar clumps.

Figure 12 shows almost the same normalized l-profiles shown in Figure 11 for the star-forming populations of WISE H II regions and ATLASGAL clumps together with FUGIN ^{12}CO (1–0) and COHRS ^{12}CO (3–2). The histograms of the star-forming populations were obtained by counting the number of sources from each
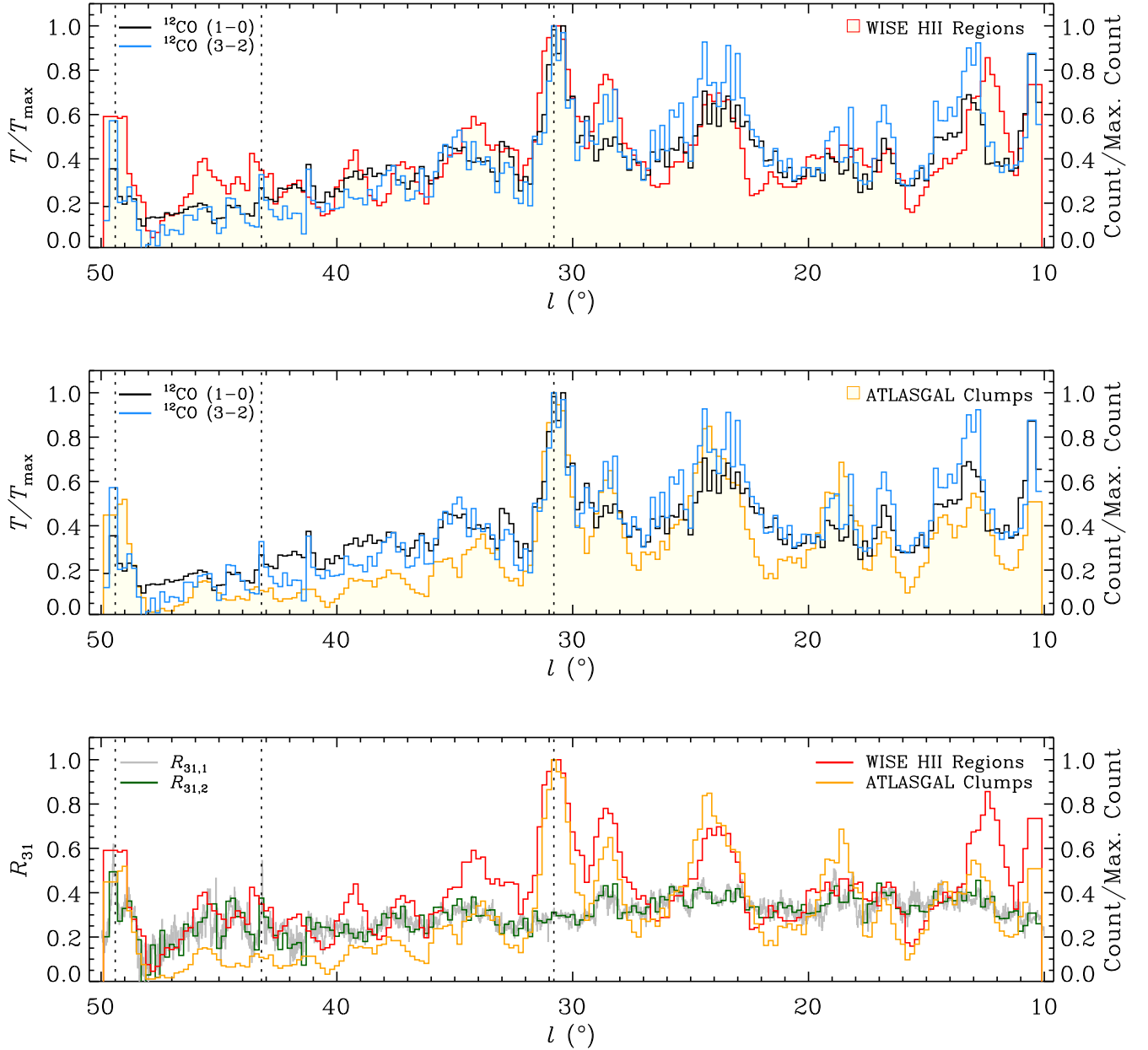
Figure 12. Integrated l distribution of ^{12}CO (1–0) (FUGIN; black), ^{12}CO (3–2) (COHRS; blue), Galactic H II regions (WISE; red in the top and bottom panels), star-forming clumps (ATLASGAL; orange in the middle and bottom panels), and the line ratio R_{31} (gray and green in the bottom panel). Each profile is integrated over $b \leqslant 0°5$ and $-60 \text{ km s}^{-1} < v_{\text{LSR}} < +170 \text{ km s}^{-1}$. The star-forming clumps comprise all clumps except starless ones in the ATLASGAL compact-source catalog, that is, MSF clumps, YSO-forming clumps, and protostellar clumps. The CO histograms are drawn in the same way as in Figure 11, but are interpolated to have the same bin size (12′) and abscissa values as those of the H II regions and star-forming clumps. For the H II regions and star-forming clumps, each histogram was obtained by counting the number of sources in a moving bin with a population-counting bin width of 1° and a moving-bin interval of 12′. The green profile ($R_{31,2}$) is the ratio of the two CO transition profiles in the upper panels, but on an absolute scale that is not normalized by the maximum. Likewise, the gray profile ($R_{31,1}$) is the ratio on the absolute scale of the two CO profiles shown in Figure 11. Three vertical dotted lines are drawn to help locate three star-forming regions: W43 ($l = 30°8$), W49A ($43°2$), and W51 ($49°4$).

catalog in the moving bin with a bin size of 1° and a step size of 12′. These moving-bin histograms avoid bias due to a specific bin size. For statistical comparative analysis, the two CO emission profiles were interpolated using the IDL INTERPOL function to have a bin size (12′) equal to that of the star-forming population profiles. In the given longitude range, all profiles reach their largest peak at the longitudes in the W43 direction (30°8). At the longitudes in the W51 direction (49°4), all of them also show a distinct peak. However, near the W49A (43°2) direction, the peak height decreases significantly with smoothing. At $l = 49°5$, the ^{12}CO (3–2), WISE H II regions, and ATLASGAL clumps show a

huge excess compared to ^{12}CO (1–0), which can indicate a very high temperature of CO due to high star-forming activity, while at $l = 30°$, all four distributions exhibit similar intensities.

In addition, a broad hump centered around $l \sim 24°$ stands out. The distribution of ^{12}CO (3–2) shows three thin and sharp peaks, one of which coincides with the peak of the ATLASGAL clumps. However, the distributions of ^{12}CO (1–0) and WISE H II regions are relatively smooth. The G24° hump is seen as a combination of WISE H II regions/GMCs close to each other in the longitude direction—for example, GMCs with MSF activity such as G23.01−0.41 at $\sim 77 \text{ km s}^{-1}$, G23.44−0.18 at $\sim 100 \text{ km s}^{-1}$, and
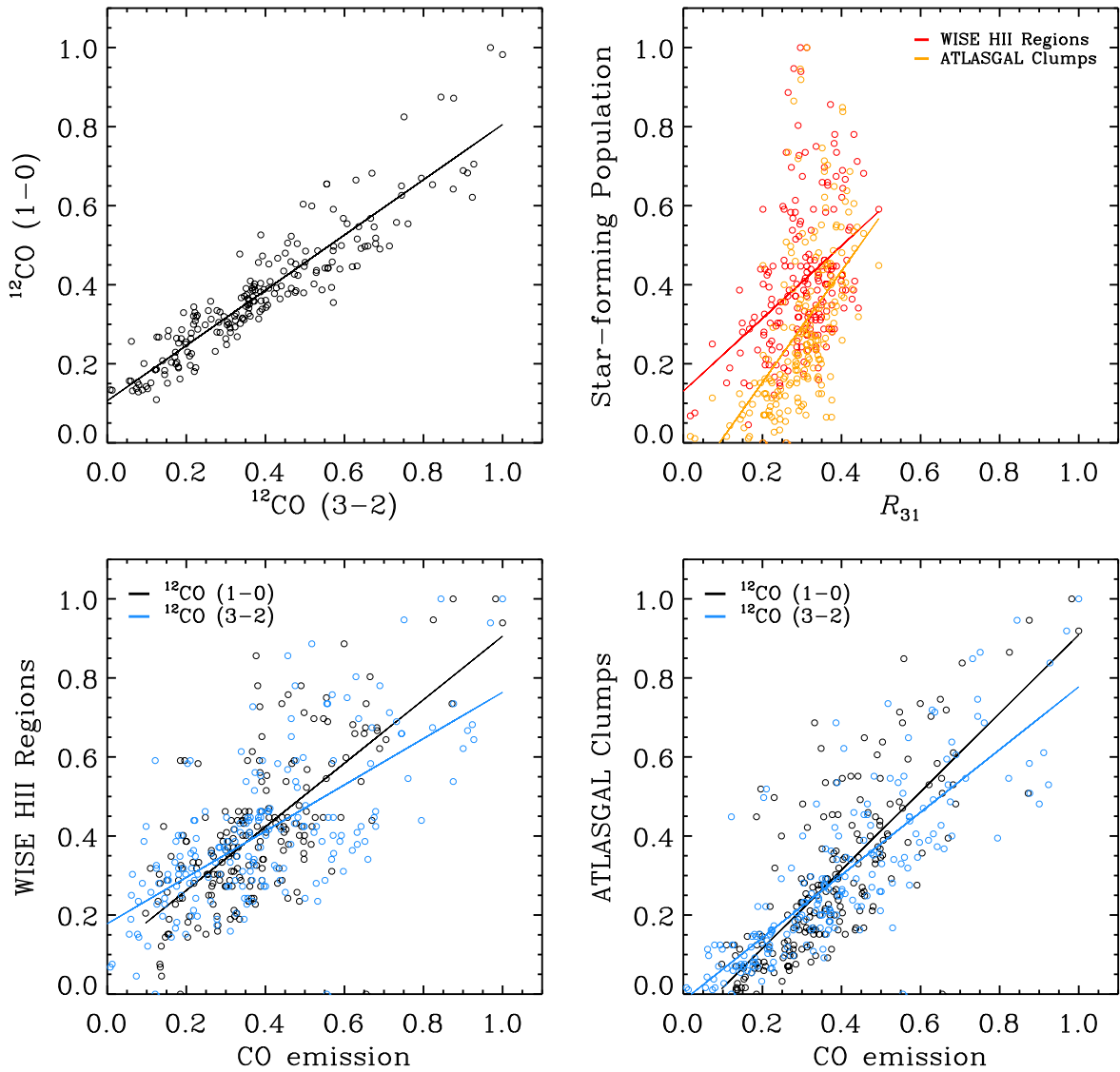
Figure 13. Scatterplots between two targets using the normalized histogram values shown in Figure 12: clockwise from top left, ^{12}CO (1–0) vs. ^{12}CO (3–2), WISE H II regions (red) or ATLASGAL star-forming clumps (orange) vs. R_{31}, star-forming clumps vs. CO emission, and WISE H II regions vs. CO emission. In the two bottom panels, ^{12}CO (1–0) and ^{12}CO (3–2) are displayed with black and blue circles, respectively. A solid line is the best result of a least-squares fit in a linear model using the IDL LINFIT procedure.

G25.38−0.18 (W42) at ∼65 km s^{-1} (e.g., Brunthaler et al. 2009; Ohishi et al. 2012; Dewangan et al. 2015; Su et al. 2015). This incredibly rich line of sight is being targeted for the GASTON Galactic plane survey (Rigby et al. 2021). Interestingly, the distribution of WISE H II regions shows a strong peak at about 12°.5, but not present in the other distributions. The peak does not appear when counting only objects that have a single measured velocity, marked in Figure 6. About half of the WISE H II regions contributing to the peak do not have measured velocity information and most of them are classified as radio-quiet sources. This area might contain many old WISE H II regions that have dispersed the molecular clouds they were formed in.

We estimated the line ratio of the two CO transitions, i.e., $R_{31} \equiv$ ^{12}CO (3–2)/^{12}CO (1–0). The R_{31} l distribution with two different bin sizes is displayed in the bottom panel of Figure 12 and compared to the WISE H II regions and ATLASGAL clumps. For R_{31}, the gray profile ($R_{31,1}$) has the same 60″ bin size as the CO l-profile in Figure 11, and the green profile ($R_{31,2}$) has the same 12′ bin size as the other profiles in Figure 12. We found a median $R_{31} = 0.27$, which is similar to the mean value of 0.31 for

nearby galaxies (Leroy et al. 2022). Compared to the CO profiles normalized by the maximum shown in the upper panels, the R_{31} profile shows less dramatic variation except near the W51 direction (see Figure 13 also). At $l = 48°.2$, a deep valley is visible, with the higher-longitude side increasing more steeply than the lower-longitude one. At $l = 49°.4$, W51's line of sight, the R_{31} profile is peaked ($R_{31,2} = 0.50$).

A scatterplot was drawn for each pair, as shown in Figure 13, and the Spearman correlation test was applied to evaluate the relationship of the results. We used `pymccorrelation`[21] of Privon et al. (2020), which is a Python implementation and expansion of a Monte Carlo error analysis procedure described by Curran (2014). We computed the Spearman correlation coefficient (ρ) using 1000 bootstrapping iterations, and the median and 16th/84th percentile ranges are listed in Table 2. A $\rho = +1$ or -1 is a perfect positive or negative correlation while $\rho = 0$ is indicative of no correlation between the data. For the two CO transitions, ρ is 0.94. It is not surprising that they show

---

[21] https://github.com/privong/pymccorrelation

Table 2
Spearman Correlation Coefficients

	COHRS	FUGIN	$R_{31,2}$	ATLASGAL
FUGIN	$0.94^{+0.01}_{-0.01}$	⋯	⋯	⋯
WISE	$0.65^{+0.05}_{-0.05}$	$0.65^{+0.05}_{-0.05}$	$0.42^{+0.06}_{-0.06}$	$0.81^{+0.03}_{-0.03}$
ATLASGAL	$0.84^{+0.03}_{-0.03}$	$0.76^{+0.04}_{-0.05}$	$0.66^{+0.05}_{-0.05}$	⋯

Note. These are the 50% value and 16%/84% range of the coefficient probability distribution obtained by bootstrapping with 1000 iterations.

a very strong positive correlation. There is also a positive correlation between CO and the existence of the star-forming populations. As the ATLASGAL clumps used in this paper were only those that form stars, it is natural that there is a strong positive correlation between WISE and ATLASGAL (WISE–ATLASGAL). On the other hand, the ATLASGAL clumps show a stronger correlation with CO or $R_{31,2}$ than the WISE H II regions. That is because the ATLASGAL catalog contains sources in earlier evolution stages than the WISE catalog, which are still deeply embedded in their natal molecular cloud. Comparing the relationships between the two transitions and the ATLASGAL clumps, the COHRS–ATLASGAL correlation coefficient is greater than the FUGIN–ATLASGAL correlation coefficient. Also, the difference in correlation coefficient between COHRS–WISE and COHRS–ATLASGAL is larger than that between FUGIN–WISE and FUGIN–ATLASGAL. These are explained by ^{12}CO (3–0) being more sensitive to dense gas than ^{12}CO (1–0). In addition, the COHRS–ATLASGAL correlation is slightly stronger than WISE–ATLASGAL. Thus, the $J = (3–2)$ transition is a better tracer of star-forming gas.

8. Summary

We present the full data of COHRS, which is a survey mapping a region of the Galactic plane covering $9°5 \leqslant l \leqslant 62°3$ and $|b| \leqslant 0°5$ in ^{12}CO (3–2) using HARP on the JCMT. Since the initial public release of Paper I, further observations have been made to reach the full scope of the survey, and improved data reduction processes have been applied, including steps to mitigate off-position contamination effects. The COHRS data are publicly accessible at doi:10.11570/22.0078. The released data have an angular resolution of $16''6$ and a velocity resolution of $0.635 \, \mathrm{km \, s^{-1}}$ with a velocity coverage of $-200 \, \mathrm{km \, s^{-1}} < v_{\mathrm{LSR}} < +300 \, \mathrm{km \, s^{-1}}$. The data are sampled on $6''$ pixels and have a mean rms of 0.6 K.

We investigate the integrated one-dimensional distribution of COHRS ^{12}CO (3–2) and compare it with those of FUGIN ^{12}CO (1–0) and star-forming populations (WISE H II regions and ATLASGAL star-forming clumps). When comparing them in the integrated longitudinal space, the peak locations are generally similar to each other, but differences in peak intensity can be seen in many longitudes. For example, the distinct peak of $l = 12°5$, visible only in WISE H II regions, suggests that old star-forming regions are distributed in the line of sight and the surrounding molecular gas has already been blown away. All available pairs (^{12}CO (1–0) versus ^{12}CO (3–2) and WISE H II regions or ATLASGAL star-forming clumps versus R_{31} or CO emission) present a positive correlation. The relationship between ^{12}CO (3–2) and ATLASGAL clumps is slightly stronger than that between ^{12}CO (3–2) and WISE H II regions, while the relationships between ^{12}CO (1–0) and the two star formation tracers are relatively similar. This can happen because the higher CO transition traces denser areas within molecular clouds and is more closely related to early star formation stages.

The COHRS data will be complemented with existing and upcoming CO and continuum surveys to study statistical properties of molecular gases along the Galactic plane as well as detailed structures and properties of individual objects. These high-resolution data of molecular gas will also help us to investigate outflow activity in star-forming regions. Methanol masers are an unambiguous indicator of massive star formation, and Green et al. (2010) and Breen et al. (2015) have provided unbiased 6 GHz class II methanol maser surveys in the COHRS area. In future work, we will investigate outflow features toward massive star-forming regions where methanol masers are detected.

Appendix A
Parameters for QA

For an observation to be included in the group phase of the ORAC-DR reduction, a number of QA criteria have to be met.

These are listed below. Brief descriptions of the parameters may be found in Thomas et al. (2018, Appendix H).

```
BADPIX_MAP = 0.3
GOODRECEP = 10
TSYSBAD = 2000
FLAGTSYSBAD = 0.5
TSYSMAX = 1500
TSYSVAR = 1.0
RMSVAR_RCP = 1.0
RMSVAR_SPEC = 0.4
RMSVAR_MAP = 2.0
RMSTSYSTOL = 0.5
RMSTSYSTOL_QUEST = 0.15
RMSTSYSTOL_FAIL = 0.2
RMSMEANTSYSTOL = 1.0
CALPEAKTOL = 0.2
CALINTTOL = 0.2
RESTOL = 1
RESTOL_SM = 1
```

Given that the COHRS data were obtained in poor observing conditions, some with 225 GHz opacity greater than 0.3, we chose a relaxed maximum T_{sys} to be more inclusive, to permit noisy data to be combined with repeat observations of similar quality.

Appendix B
Example Recipe Parameter File

Fine control of ORAC-DR recipes may be achieved through recipe parameters. Every region observed in COHRS has an associated recipe file. Below is an annotated example, reordered for convenience. Boolean parameters were assigned 1 for true or 0 for false. Spectral channel ranges were all measured in kilometers per second.

```
[REDUCE_SCIENCE_NARROWLINE]
#
# MAKECUBE parameters
#
CUBE_WCS = GALACTIC
PIXEL_SCALE = 6.0
SPREAD_METHOD = Gauss
SPREAD_WIDTH = 9
SPREAD_FWHM_OR_ZERO = 6
#
# Tiling and chunking
#
TILE = 0
CHUNKSIZE = 12288
CUBE_MAXSIZE = 1536
#
# Baseline
#
BASELINE_ORDER = 1
```

The above apply to the REDUCE_SCIENCE_NARROWLINE recipe, and are constant for all the parameter files. The first stanza controlled how the PPV spectral cubes were sampled as described in Section 2.2. The middle group was not essential, but it allowed the PPV cube to be made as one, rather than being fragmented into chunks. The final parameter defined the baseline-fitting polynomial order. See Section 2.2.

```
#
# Bad-baseline filtering
#
BASELINE_LINEARITY = 1
BASELINE_LINEARITY_LINEWIDTH = -25:87
BASELINE_LINEARITY_MINRMS = 0.080
HIGHFREQ_INTERFERENCE = 1
HIGHFREQ_RINGING = 0
HIGHFREQ_INTERFERENCE_THRESH_CLIP = 4.0
LOWFREQ_INTERFERENCE = 1
```

These parameters decided which tests were performed on the raw data to reject spectra containing significant nonastronomical signals. All observations' processing tested that baselines were not grossly deviant from linearity, both for individual spectra (LOWFREQ_INTERFERENCE) and for each receptor as a whole (BASELINE_LINEARITY). The QA also searched for spectra with alternating abnormally bright and dark fluxes (HIGHFREQ_INTERFERENCE). HIGHFREQ_RINGING was only enabled if ringing (Jenness et al. 2015) was detected in Receptor H07. BASELINE_LINEARITY_LINEWIDTH specified a velocity range to exclude from the nonlinearity tests. When the astronomical emission was not restricted to a single range, we set BASELINE_LINEARITY_LINEWIDTH=base to request that BASELINE_REGIONS be used instead to define the velocity ranges to *include* in the tests. BASELINE_LI-NEARITY_MINRMS was the minimum rms deviation from linearity, measured in antenna temperature, for a receptor to be flagged as bad. Well-behaved data had rms values that ranged from 0.01 to 0.03. HIGHFREQ_INTERFERENCE_THRESH_-CLIP set the number of standard deviations at which to threshold the noise profile of raw spectra above its median level, in order to decide whether to reject spectra with high-frequency noise.

```
#
# Flatfield receptors
#
FLATFIELD = 1
FLAT_METHOD = sum
FLAT_RE-
GIONS = 12.0:25.2,27.2:29.1,35.7:41.5
```

These parameters defined whether or not to flat-field (FLATFIELD)—always performed with the summation method FLAT_METHOD, which proved to be the most stable —and the list of velocity ranges over which to integrate the fluxes for each receptor. If FLATFIELD=0, the subsequent flat-field parameters were ignored.

```
#
#  Reference-spectrum  removal  from  time-
series cubes
# ---Automatic
#
SUBTRACT_REF_EMISSION = 1
CLUMP_METHOD = clumpfind
REF_EMISSION_MASK_SOURCE = both
REF_EMISSION_COMBINE_REFPOS = 1
REF_EMISSION_BOXSIZE = 19
#
# ---Manual location
#
SUBTRACT_REF_SPECTRUM = 1
```

19

```
REF_SPECTRUM_COMBINE_REFPOS = 1
REF_SPECTRUM_REGIONS = -
1.5:0.1,2.5:4.0,7.0:11.1
```

The reference (off) position for the majority of the observed regions contained emission that appears as absorption features in all spectra. When it was detected after inspection of the first-pass reductions of the PPV cubes, the removal techniques were enabled by switching on SUBTRACT_REF_SPECTRUM. We did not want any unnecessary modification of spectra where no evident off position was visible.

An outline of the methods used can be found in Section 2.2.1. The first stanza defined parameters for the automated method. REF_EMISSION_MASK_SOURCE used not only the source-masked spectrum to locate the lines, but also the unmasked modal spectrum to determine the line strengths. The emission was located with the ClumpFind algorithm (Williams et al. 2011) applied in one dimension by FINDCLUMPS from the CUPID (Berry et al. 2007) package. In rare circumstances where repeat observations had switched reference positions, each reference position was analyzed separately (REF_EMISSION_COMBINE_REFPOS).

The second stanza was to deal with residual off-position signals that the automated method left, being either untouched lines or, most commonly, lines reduced in depth but not eliminated. Application of this algorithm was enabled by SUBTRACT_REF_SPECTRUM. REF_SPECTRUM_COMBI-NE_REFPOS performed the equivalent action as REF_EMIS-SION_COMBINE_REFPOS. A list of the line extents was supplied through REF_SPECTRUM_REGIONS.

In the seven cases where even the manual guidance did not remove all the absorption lines, the name of a manually determined off-position residual spectrum was supplied through REF_SPECTRUM_FILE (not shown above).

```
#
# Properties of final products
#
FINAL_LOWER_VELOCITY = -230
FINAL_UPPER_VELOCITY = 355
REBIN = 0.635,1.0
```

The velocity limits of the PPV cubes were set by the first two recipe parameters. These limits were further trimmed during mosaic formation in order to prevent exceeding the maximum number of array elements. REBIN assigned velocity resolutions for regridded PPV cubes, generating one at the R2 width of $0.635\,\mathrm{km\,s^{-1}}$, and the other at $1.0\,\mathrm{km\,s^{-1}}$ width for comparison with R1.

```
#
# Moment maps
#
MOMENTS_LOWER_VELOCITY = -43
MOMENTS_UPPER_VELOCITY = 84
LV_IMAGE = 1
LV_AXIS = skylat
LV_ESTIMATOR = sum
```

For completeness, the final set of parameters asked for the creation of a longitude–velocity (LV) map, summing over Galactic latitude. These LV maps were for quick inspections of the reductions, and do not form part of the release. The released LV maps were derived from the mosaics. The first two parameters restricted the velocity range when computing the moment maps, and were used for efficiency.

Appendix C
Automated Algorithm for Removal of Off-position Signals

This appendix expands on the outline, presented in Section 2.2.1, of the automated algorithm to remove off-position signals.

1. Data observed at different reference positions are processed separately.
2. The initial step is to collapse the time axis by forming the mode at each spectral channel. Those modal spectra are mildly smoothed with a 1.5-channel FWHM Gaussian point-spread function in order to define the extent of the absorption lines better. The mode at each spectral channel is determined by an iterative maximum likelihood function, for which the data are inversely weighted by their deviations from the current mean. At each iteration outliers at 3.0 standard deviations from the current mean are clipped. Iterations proceed until convergence to a stationary point.
3. Refinement of the modal spectra occurs for each receptor as follows.
   a. The lines under analysis are always in emission, as required by the clump-finding software.
   b. Before the locations of reference-spectrum emission lines are determined within the masked-source modal spectrum, an attempt to remove residual source emission is made. Its steps are as follows: subtract a 75 pixel median-smoothed version, then mask channels that fall below a $-3 \times$ rms threshold, then repeat the first step but with the kernel reduced to 41 pixels.
   c. In the search for off-position lines the background is not initially subtracted. While this choice may lose weaker reference emission embedded in extended source signals, it compensates by not regarding dips in the source signal as reference emission.
   d. Line properties come from CUPID's FINDCLUMPS with a tuned ClumpFind method, with a $2 \times$ rms minimum detection level. Consequently, to allow for wings near the baseline, an additional three pixels on either side of the line are masked. A fixed 19-channel smoothing kernel is used to determine the background for the line finding (but there is an option to measure the widest line iteratively in order to set the smoothing kernel).
   e. The masked channels for the reference and the source are applied to each unmasked modal spectrum, which is analyzed in the same fashion as that for the masked modal spectrum.
   f. Any residual background from spectrally broad source emission is removed with FINDBACK from the CUPID package once the masked channels are filled using an iterated solution to Laplace's equation. The revised background is more accurate as the bulk of the emission and off-position lines have been excised.
   g. The properties of reference lines are measured once again, now improved by the more accurate background.
   h. Any varying residual background is removed to cater for spectrally extended source emission. A narrow (nine-channel) kernel is used to track the background more precisely.
   i. A bias remains in the background subtraction and a $1.5 \times$ rms empirical correction is added.
   j. Masked values beyond the spectral lines in the estimated reference spectrum are set to zero.

4. For data taken at different epochs, the mapping from pixel to velocity is likely to be different, so they are aligned to the first epoch. This permits pixel-by-pixel subtraction.
5. The estimated reference spectrum is expanded to the bounds of the raw time series, from which the spectrum is subtracted.

Appendix D
Average rms Noise Levels of COHRS Tiles

Table D1 provides the name and mean rms noise of each COHRS tile.

Table D1
COHRS Tile Summary

#	Tile Name[a]	rms Noise[b] (K)
1	COHRS_09p50_0p00	0.84
2	COHRS_10p00_0p00	0.72
3	COHRS_10p50_0p00	0.33
4	COHRS_11p00_0p00	0.72
5	COHRS_11p50_0p00	0.33
6	COHRS_12p00_0p00	0.38
7	COHRS_12p50_0p00	0.52
8	COHRS_13p00_0p00	0.37
9	COHRS_13p50_0p00	0.63
10	COHRS_14p00_0p00	0.36
11	COHRS_14p50_0p00	0.51
12	COHRS_15p00_0p00	0.31
13	COHRS_15p50_0p00	0.42
14	COHRS_16p00_0p00	0.39
15	COHRS_16p50_0p00	0.37
16	COHRS_17p00_0p00	0.70
17	COHRS_17p50_0p00	0.90
18	COHRS_18p00_0p00	0.74
19	COHRS_18p50_0p00	0.64
20	COHRS_19p00_0p00	0.85
21	COHRS_19p50_0p00	0.78
22	COHRS_20p00_0p00	0.61
23	COHRS_20p50_0p00	0.43
24	COHRS_21p00_0p00	0.65
25	COHRS_21p50_0p00	0.75
26	COHRS_22p00_0p00	0.76
27	COHRS_22p50_0p00	0.72
28	COHRS_23p00_0p00	0.58
29	COHRS_23p50_0p00	0.53
30	COHRS_24p00_0p00	0.56
31	COHRS_24p50_0p00	0.52
32	COHRS_25p00_0p00	0.52
33	COHRS_25p50_0p00	0.40
34	COHRS_26p00_0p00	0.47
35	COHRS_26p50_0p00	0.61
36	COHRS_27p00_0p00	0.64
37	COHRS_27p50_0p00	0.53
38	COHRS_28p00_0p00	0.46
39	COHRS_28p50_0p00	0.52
40	COHRS_29p00_0p00	0.47
41	COHRS_29p50_0p00	0.46
42	COHRS_30p00_0p00	0.60
43	COHRS_30p50_0p00	0.50
44	COHRS_31p00_0p00	0.68
45	COHRS_31p50_0p00	0.76
46	COHRS_32p00_0p00	0.56
47	COHRS_32p50_0p00	0.50
48	COHRS_33p00_0p00	0.44

Table D1
(Continued)

#	Tile Name[a]	rms Noise[b] (K)
49	COHRS_33p50_0p00	0.53
50	COHRS_34p00_0p00	0.46
51	COHRS_34p50_0p00	0.47
52	COHRS_35p00_0p00	0.42
53	COHRS_35p50_0p00	0.43
54	COHRS_36p00_0p00	0.44
55	COHRS_36p50_0p00	0.51
56	COHRS_37p00_0p00	0.50
57	COHRS_37p50_0p00	0.44
58	COHRS_38p00_0p00	0.49
59	COHRS_38p50_0p00	0.44
60	COHRS_39p00_0p00	0.56
61	COHRS_39p50_0p00	0.57
62	COHRS_40p00_0p00	0.49
63	COHRS_40p50_0p00	0.52
64	COHRS_41p00_0p00	0.48
65	COHRS_41p50_0p00	0.58
66	COHRS_42p00_0p00	0.76
67	COHRS_42p50_0p00	0.66
68	COHRS_43p00_0p00	0.57
69	COHRS_43p50_0p00	0.21
70	COHRS_44p00_0p00	0.48
71	COHRS_44p50_0p00	0.50
72	COHRS_45p00_0p00	0.54
73	COHRS_45p50_0p00	0.52
74	COHRS_46p00_0p00	0.59
75	COHRS_46p50_0p00	0.61
76	COHRS_47p00_0p00	0.70
77	COHRS_47p50_0p00	0.82
78	COHRS_48p00_0p00	0.78
79	COHRS_48p50_0p00	0.59
80	COHRS_49p00_0p00	0.71
81	COHRS_49p50_0p00	0.67
82	COHRS_50p00_0p00	0.76
83	COHRS_50p50_0p00	0.62
84	COHRS_51p00_0p00	0.58
85	COHRS_51p50_0p00	0.38
86	COHRS_52p00_0p00	0.73
87	COHRS_52p50_0p00	1.01
88	COHRS_53p00_0p00	0.61
89	COHRS_53p50_0p00	0.80
90	COHRS_54p00_0p00	0.48
91	COHRS_54p50_0p00	0.58
92	COHRS_55p00_0p00	0.56
93	COHRS_55p50_0p00	0.67
94	COHRS_56p00_0p00	0.52
95	COHRS_56p50_0p00	0.47
96	COHRS_57p00_0p00	0.72
97	COHRS_57p50_0p00	0.46
98	COHRS_58p00_0p00	0.67
99	COHRS_58p50_0p00	0.89
100	COHRS_59p00_0p00	0.94
101	COHRS_59p50_0p00	0.50
102	COHRS_60p00_0p00	0.49
103	COHRS_60p50_0p00	0.77
104	COHRS_61p00_0p00	0.73
105	COHRS_61p50_0p00	0.99
106	COHRS_62p00_0p00	0.81

Notes.
[a] The numbers in the tile name give the central longitude and latitude of the tile.
[b] The mean T_A^* rms noise in the tiles rebinned to a 0.635 km s^{-1} channel width.

ORCID iDs

Geumsook Park (박금숙) ⓘ https://orcid.org/0000-0001-8467-3736

Malcolm J. Currie ⓘ https://orcid.org/0000-0003-0141-0362

Holly S. Thomas ⓘ https://orcid.org/0000-0003-1008-5477

Erik Rosolowsky ⓘ https://orcid.org/0000-0002-5204-2259

Jessica T. Dempsey ⓘ https://orcid.org/0000-0002-5457-9025

Kee-Tae Kim ⓘ https://orcid.org/0000-0003-2412-7092

Andrew J. Rigby ⓘ https://orcid.org/0000-0002-3351-2200

David J. Eden ⓘ https://orcid.org/0000-0002-5881-3229

Harriet Parsons ⓘ https://orcid.org/0000-0002-6327-3423

References

Aguirre, J. E., Ginsburg, A. G., Dunham, M. K., et al. 2011, ApJS, 192, 4
Alves, J., & Homeier, N. 2003, ApJL, 589, L45
Anderson, L. D., Bania, T. M., Balser, D. S., et al. 2014, ApJS, 212, 1
Anderson, L. D., Wenger, T. V., Armentrout, W. P., Balser, D. S., & Bania, T. M. 2019, ApJ, 871, 145
Anderson, L. D., Bania, T. M., Balser, D. S., et al. 2020, WISE Catalog of Galactic HII Regions, v2.2, NASA/IPAC Infrared Science Archive, doi:10.26131/IRSA146
Banerjee, R., & Pudritz, R. E. 2006, ApJ, 641, 949
Benjamin, R. A., Churchwell, E., Babler, B., et al. 2003, PASP, 115, 953
Berry, D. S., Reinhold, K., Jenness, T., & Economou, F. 2007, in ASP Conf. Ser. 376, Astronomical Data Analysis Software and Systems XVI, ed. R. A. Shaw, F. Hill, & D. J. Bell (San Francisco, CA: ASP), 425
Bertin, E., Mellier, Y., Radovich, M., et al. 2002, in ASP Conf. Ser. 281, Astronomical Data Analysis Software and Systems XI, ed. D. A. Bohlender, D. Durand, & T. H. Handley (San Francisco, CA: ASP), 228
Bolatto, A. D., Wolfire, M., & Leroy, A. K. 2013, ARA&A, 51, 207
Breen, S. L., Fuller, G. A., Caswell, J. L., et al. 2015, MNRAS, 450, 4109
Brunthaler, A., Reid, M. J., Menten, K. M., et al. 2009, ApJ, 693, 424
Buckle, J. V., Hills, R. E., Smith, H., et al. 2009, MNRAS, 399, 1026
Carpenter, J. M., & Sanders, D. B. 1998, AJ, 116, 1856
Carey, S. J., Noriega-Crespo, A., Mizuno, D. R., et al. 2009, PASP, 121, 76
Chapin, E., Gibb, A. G., Jenness, T., et al. 2013, Starlink User Note, 258
Churchwell, E., Babler, B. L., Meade, M. R., et al. 2009, PASP, 121, 213
Colombo, D., Rosolowsky, E., Duarte-Cabral, A., et al. 2019, MNRAS, 483, 4291
Colombo, D., Rosolowsky, E., Ginsburg, A., Duarte-Cabral, A., & Hughes, A. 2015, MNRAS, 454, 2067
Contreras, Y., Schuller, F., Urquhart, J. S., et al. 2013, A&A, 549, A45
Curran, P. A. 2014, arXiv:1411.3816
Currie, M. J., & Berry, D. S. 2013, Starlink User Note, 95
Currie, M. J., Berry, D. S., Jenness, T., et al. 2014, in ASP Conf. Ser. 485, Astronomical Data Analysis Software and Systems XXIII, ed. N. Manset & P. Forshay (San Francisco, CA: ASP), 391
Curtis, E. I., Richer, J. S., & Buckle, J. V. 2010, MNRAS, 401, 455
Dame, T. M., Hartmann, D., & Thaddeus, P. 2001, ApJ, 547, 792
Dame, T. M., & Thaddeus, P. 1985, ApJ, 297, 751
Dempsey, J. T., Thomas, H. S., & Currie, M. J. 2013, ApJS, 209, 8, (Paper I)
Dewangan, L. K., Luna, A., Ojha, D. K., et al. 2015, ApJ, 811, 79
Eden, D. J., Moore, T. J. T., Currie, M. J., et al. 2020, MNRAS, 498, 5936
Eden, D. J., Moore, T. J. T., Plume, R., et al. 2017, MNRAS, 469, 2163
Eden, D. J., Moore, T. J. T., Urquhart, J. S., et al. 2018, MNRAS, 477, 3369

Galvan-Madrid, R., Liu, H. B., Zhang, Z.-Y., et al. 2013, ApJ, 779, 121
Gibb, A. G., Jenness, T., & Economou, F. 2013, Starlink User Note, 265
GLIMPSE Team 2020, GLIMPSE I Archive, NASA/IPAC Infrared Science Archive, doi:10.26131/IRSA210
Green, J. A., Caswell, J. L., Fuller, G. A., et al. 2010, MNRAS, 409, 913
Gaudet, S., Dowler, P., Goliath, S., et al. 2009, in ASP Conf. Ser. 411, Astonomical Data Analysis Software and Systems XVIII, ed. D. A. Bohlender, D. Durand, & P. Dowler (San Francisco, CA: ASP), 185
Jackson, J. M., Rathborne, J. M., Shah, R. Y., et al. 2006, ApJS, 163, 145
Jenness, T., Currie, M. J., Tilanus, R. P. J., et al. 2015, MNRAS, 453, 73
Jenness, T., & Economou, F. 2015, A&C, 9, 40
Kang, M., Bieging, J. H., Kulesa, C. A., et al. 2010, ApJS, 190, 58
Karim, T., & Mamajek, E. E. 2017, MNRAS, 465, 472
Kohno, M., Tachihara, K., Torii, K., et al. 2021, PASJ, 73, S129
Landsman, W. B. 1993, in ASP. Conf. Ser. 52, Astronomical Data Analysis Software and Systems II, ed. R. J. Hanisch, R. J. V. Brissenden, & J. Barnes (San Francisco, CA: ASP), 246
Leroy, A. K., Rosolowsky, E., Usero, A., et al. 2022, ApJ, 927, 149
Li, Q., Zhou, J., Esimbek, J., et al. 2018, ApJ, 867, 167
Molinari, S., Swinyard, B., Bally, J., et al. 2010, PASP, 122, 314
Moore, T. J. T., Plume, R., Thompson, M. A., et al. 2015, MNRAS, 453, 4264
Motte, F., Schilke, P., & Lis, D. C. 2003, ApJ, 582, 277
Nguyen Luong, Q., Motte, F., Schuller, F., et al. 2011, A&A, 529, A41
Ohishi, Y., Sorai, K., & Habe, A. 2012, PASJ, 64, 74
Privon, G. C., Ricci, C., Aalto, S., et al. 2020, ApJ, 893, 149
Reid, M. J., Dame, T. M., Menten, K. M., & Brunthaler, A. 2016, ApJ, 823, 77
Reid, M. J., Menten, K. M., Brunthaler, A., et al. 2019, ApJ, 885, 131
Rigby, A. J., Moore, T. J. T., Plume, R., et al. 2016, MNRAS, 456, 2885
Rigby, A. J., Peretto, N., Adam, R., et al. 2021, MNRAS, 502, 4576
Sanders, D. B., Clemens, D. P., Scoville, N. Z., & Solomon, P. M. 1986, ApJS, 60, 1
Sato, M., Reid, M. J., Brunthaler, A., & Menten, K. M. 2010, ApJ, 720, 1055
Schuller, F., Csengeri, T., Urquhart, J. S., et al. 2017, A&A, 601, A124
Schuller, F., Menten, K. M., Contreras, Y., et al. 2009, A&A, 504, 415
Simon, R., Jackson, J. M., Clemens, D. P., Bania, T. M., & Heyer, M. H. 2001, ApJ, 551, 747
Su, Y., Sun, Y., Li, C., et al. 2016, ApJ, 828, 59
Su, Y., Yang, J., Zhang, S., et al. 2019, ApJS, 240, 9
Su, Y., Zhang, S., Shao, X., & Yang, J. 2015, ApJ, 811, 134
Thomas, H. S., Currie, M. J., & Parsons, H. A. L. 2018, Starlink Cookbook 20, http://www.starlink.ac.uk/docs/sc20.htx/sc20ap8.html
Umemoto, T., Minamidani, T., Kuno, N., et al. 2017, PASJ, 69, 78
Urquhart, J. S., Csengeri, T., Wyrowski, F., et al. 2014a, A&A, 568, A41
Urquhart, J. S., Figura, C. C., Moore, T. J. T., et al. 2014b, MNRAS, 437, 1791
Urquhart, J. S., König, C., Giannetti, A., et al. 2018, MNRAS, 473, 1059
Vallee, J. P. 2017, AstRv, 13, 113
van der Walt, S., Colbert, S. C., & Varoquaux, G. 2011, CSE, 13, 22
Virtanen, P., Gommers, R., Oliphant, T. E., et al. 2020, NatMe, 17, 261
Welch, W., Dreher, J. W., Jackson, J. M., Terebey, S., & Vogel, S. N. 1987, Sci, 238, 1550
Williams, J. P., de Geus, E. J., & Blitz, L. 2011, Astrophysics Source Code Library, Clumpfind: Determining Structure in Molecular Clouds, ascl:1107.014
Wright, E. L., Eisenhardt, P. R. M., Mainzer, A. K., et al. 2010, AJ, 140, 1868
Yuan, L., Yang, J., Du, F., et al. 2022, ApJS, 261, 37
Zhang, B., Moscadelli, L., Sato, M., et al. 2014, ApJ, 781, 89
Zhang, B., Reid, M. J., Menten, K. M., et al. 2013, ApJ, 775, 79